OneFlowTraX: A User-Friendly Software for Super-Resolution Analysis of Single-Molecule Dynamics and Nanoscale Organization

Leander Rohr[1], Alexandra Ehinger[1], Luiselotte Rausch[1], Nina Glöckner Burmeister[2], Alfred J. Meixner[3], Julien Gronnier[1], Klaus Harter[1], Birgit Kemmerling[1], and Sven zur Oven-Krockhaus[1,3,*]

1 Center for Plant Molecular Biology (ZMBP), University of Tübingen, 72076 Tübingen, Germany

2 Department of Biomedicine, Aarhus University, 8000 Aarhus, Denmark

3 Institute for Physical and Theoretical Chemistry, University of Tübingen, 72076 Tübingen, Germany

***Correspondence: Sven zur Oven-Krockhaus (sven.zur-oven-krockhaus@uni-tuebingen.de)**

ABSTRACT

Super-resolution microscopy (SRM) approaches revolutionize cell biology by providing insights into the nanoscale organization and dynamics of macromolecular assemblies and single molecules in living cells. A major hurdle limiting SRM democratization is post-acquisition data analysis which is often complex and time-consuming. Here, we present OneFlowTraX, a user-friendly and open-source software dedicated to the analysis of single-molecule localization microscopy (SMLM) approaches such as single-particle tracking photoactivated localization microscopy (sptPALM). Through an intuitive graphical user interface, OneFlowTraX provides an automated all-in-one solution for single-molecule localization, tracking, as well as mobility and clustering analyses. OneFlowTraX allows the extraction of diffusion and clustering parameters of millions of molecules in a few minutes. Finally, OneFlowTraX greatly simplifies data management following the FAIR (Findable, Accessible, Interoperable, Reusable) principles. We provide a detailed step-by-step manual and guidelines to assess the quality of single-molecule analyses. Applying different fluorophores including mEos3.2, PA-GFP, and PATagRFP, we exemplarily used OneFlowTraX to analyze the dynamics of plant plasma membrane-localized proteins including an aquaporin, the brassinosteroid receptor Brassinosteroid Insensitive 1 (BRI1) and the Receptor-Like Protein 44 (RLP44).

Keywords: OneFlowTraX, software, super-resolution microscopy, localization, single-particle tracking, sptPALM, photoconvertible fluorophores, photoactivatable fluorophores, cluster analysis, plasma membrane proteins, BRI1, RLP44, plant

INTRODUCTION

All living cells regulate the dynamics and organization of molecules at the nanoscale to control their biological processes. Accordingly, appropriate methods are needed to elucidate the underlying mechanisms and functions at the molecular level. In recent years, there has been a significant focus on the plasma membrane (PM) due to its crucial role in important functions such as homeostasis and mass transport, and its primary role as a mediator of signals into and out of the cell. However, only a few techniques allow the in vivo analysis of molecules with high spatiotemporal resolution. Suitable microscopy techniques include fluorescence recovery after bleaching (FRAP) (Axelrod et al., 1976; Peters et al., 1974), fluorescence correlation spectroscopy (FCS) (Magde et al., 1972), and single-particle tracking (spt) (Manzo and Garcia-Parajo, 2015) of labeled molecules, the latter being mainly driven by the advent of super-resolution technologies such as photoactivated localization microscopy (PALM) (Betzig et al., 2006; Hess et al., 2006; Manley et al., 2008).

Imaging of single molecules in living cells is usually performed under total internal reflection (TIRF) illumination, which provides greatly enhanced contrast for a thin layer of the biological sample due to its small penetration depth of around 150 nm beyond the coverslip. However, due to the relatively thick cell wall of plant cells, their compartments, such as the PM, are not in the optimal range for TIRF. Therefore, alternative illumination methods such as highly inclined thin illumination (HiLo) (Tokunaga et al., 2008), also known as variable angle epifluorescence microscopy (VAEM) (Konopka and Bednarek, 2008), are widely used for plants. Moreover, due to the limited permeability of the cell wall, plant cell biologists cannot use organic dyes common in the animal or human field (Lelek et al., 2022) for live cell imaging but must rely on a limited selection of genetically encoded fluorophores fused to the gene of interest (Hosy et al., 2015; Jolivet et al., 2023; McKenna et al., 2019).

These technical difficulties have contributed to the fact that dynamic analysis of proteins in plant cells at very high resolution has only recently taken off. The improvement of technical possibilities in microscopy and other methods, such as

single-molecule tracking and cluster analysis, now offers data on dynamic parameters, including diffusion coefficients and nanoscale organization, especially for PM proteins (Bayle et al., 2021; Gronnier et al., 2017; Gronnier et al., 2019; Hosy et al, 2015; Jaillais and Ott, 2020; Martiniere and Zelazny, 2021; McKenna et al, 2019; Perraki et al., 2018; Smokvarska et al., 2023).

Despite the progress made in recent years, the analysis of single-molecule localization microscopy (SMLM) data remains a complicated, multistep process. First, the positions of the individual labeled membrane proteins in each image must be determined with high precision (localization), followed by the assignment of localizations across multiple images to trajectories (tracking). The mobilities or proportions of mobile/immobile proteins are then calculated from the analysis of these trajectories. Subsequently, a map of all observed single molecules localizations can be reconstituted to analyze the nanoscale organization of molecules (e.g., cluster analysis). Each of these steps has been implemented over the years with dedicated analysis software (Chenouard et al., 2014; Sage et al., 2019). Localization depends on physical camera parameters and localization algorithms that must incorporate noise statistics for the low photon counts typical of single-molecule microscopy. Tracking can be performed with a variety of algorithms, and the chosen parameters have a large impact on the data evaluation, representation and thus their interpretation. Mobility analysis is initially performed using mean square displacement (MSD) plots (Qian et al., 1991). Still, this method is not always applicable and is highly sensitive to the parameters used. Combining sptPALM data with cluster analysis is a relatively recent development; several methods have advantages and disadvantages, leading to different data evaluation, representation and interpretation. This procedural complexity and challenges prevent broader application of SMLM techniques such as sptPALM especially in plant cell biology.

Although practical guides have been published recently ~~(~~Bayle et al, 2021~~)~~, there is still a lack of software packages that guide the user through all analyses without excessive computational knowledge. The available software is usually limited to or specializes in only one of the above sub-steps, with compatibility problems between the different solutions.

In this work we present a comprehensive, all-in-one open-source, time-saving software package, named OneFlowTraX, guiding the scientist through the steps of

97 SMLM-based localization, tracking, mobility- and cluster analyses of molecules in
98 living cells, which we apply to plant cells. Moreover, the storage of the SMLM data and
99 metadata follow FAIR (Findable, Accessible, Interoperable and Reusable) principles
100 (Wilkinson et al., 2016) for scientific data management and stewardship. We explored
101 three genetically encoded fluorophores (mEos3.2, PA-GFP and PATagRFP) of
102 different photophysical characteristics, suitable for sptPALM studies in living plant
103 cells, exemplified by the temporal and spatial analysis of four different plant plasma
104 membrane proteins. The PA-GFP and PATagRFP pair will also enable dual-color
105 sptPALM applications in the future.

106 RESULTS

107 Design and properties of OneFlowTraX

108 *Purpose and workflow*

109 OneFlowTraX runs as an executable program or as an application in MATLAB
110 (Mathworks). The user is guided through several steps, including the localization of
111 single molecules, the reconstruction of single-molecule trajectories, the calculation of
112 mobility parameters, and cluster analyses based on molecule or trajectory positions.
113 The easily scriptable and customizable code is available on GitHub
114 (https://github.com/svenzok/OneFlowTraX), accompanied by a user guide that
115 answers all analysis-specific questions. For each main analysis step (localization,
116 tracking, mobility and cluster analysis), extensive literature research was conducted
117 to select the most suitable method or algorithm for OneFlowTraX. Published codes
118 were partially adapted to meet the requirements of OneFlowTraX; alternatively, new
119 software code was written to provide a robust and efficient all-in-one analysis pipeline
120 for state-of-the-art single-molecule imaging analyses. The individual steps are
121 discussed in more detail in the following sections.

122 *Localization*

123 The sptPALM raw data (Figure 1A) usually consists of time series images that are
124 saved as TIFF image stacks. Typical formats in our experiments are 100x100 to
125 400x400 pixels (corresponding to 10x10 to 40x40 µm) with 2 000 to 10 000 images
126 taken at a frame rate between 20 and 50 Hz. These parameters can vary depending
127 on the specific experiment but are mainly governed by the optimal magnification of the

128 imaging system for single-molecule detection, the choice of the frame rate that
129 achieves sufficient contrast, the size of the imaged PM region of interest, and the
130 photophysical characteristics of the chosen fluorophore.

131 In the first step, the fluorophore-tagged molecules are localized in each image with
132 high precision using algorithms developed for super-resolution microscopy. Bright
133 pixels indicate possible detected single molecules, and larger sections around these
134 pixels are fitted with a two-dimensional Gaussian (Figure 1A). This results not only in
135 the position but also the PSF size, the number of photons and the subsequently
136 calculated localization accuracy, which are stored for each localized single molecule
137 (Figure 1B). For this purpose, we adapted the core of the SMAP software (Ries, 2020).
138 Its algorithm for determining single-molecule positions uses a robust maximum
139 likelihood estimation (MLE) of Gaussian point spread function (PSF) models, which
140 was shown to be very accurate (Sage et al, 2019). Furthermore, it can make use of a
141 graphic processing unit (GPU) that massively accelerates image processing speed. In
142 addition, the fitter can also account for the pixel-specific noise of commonly used
143 complementary metal-oxide semiconductor (CMOS) cameras. In OneFlowTraX, this
144 process can be started for a list of files using default parameters (Figure 1C). An
145 auxiliary window can be opened to check the performance of the algorithm on selected
146 single images and adjust the parameters (see the user guide that is provided with the
147 software for detailed information) if necessary. At the end of the localization process,
148 three histograms show (i) the PSF sizes, (ii) photons and (iii) localization accuracy for
149 all detected and fitted molecules. These histograms can be used to check the quality
150 of the raw data and exclude outliers from further analysis, for example, localizations
151 with unusually large PSFs due to poor focusing or aggregation artifacts. After review,
152 the molecule positions can be used to define single-molecule trajectories.

153 ***Tracking***

154 The generally low localization density in sptPALM data allows for a simple but very
155 fast tracking algorithm. A trajectory is formed from all those molecule positions that do
156 not exceed a maximum distance from each other in successive images (Figure 2A).
157 In addition, short sequences are bridged in which a molecule was temporarily
158 undetectable (gap closing), which is typical of the blinking behavior of fluorophores
159 observed in single-molecule microscopy. The corresponding code for this algorithm
160 was adapted from a MATLAB program published by Jean-Yves Tinevez (Tinevez,

161 2011). The underlying Linear Assignment Problem (LAP) tracker (Jaqaman et al.,
162 2008) is also part of the widely used software TrackMate (Tinevez et al., 2017). After
163 performing the tracking in OneFlowTraX, the resulting trajectories can be visualized
164 (Figure 2B, upper right), and colored according to their duration, displacement,
165 mobility and other characteristics. In case of obvious connection errors (see the user
166 guide for examples), the tracking can be repeated with adjusted track-building
167 parameters.

168 ***Mobility analysis***

169 The mean square displacement (MSD) analysis is currently the most widely used
170 method for extracting diffusion coefficients and motion patterns for this type of data
171 (Manzo and Garcia-Parajo, 2015). Therefore, the distances a molecule has traveled
172 in certain time intervals is assessed to calculate mobility metrics like the diffusion
173 coefficient (Figure 2A). A more detailed description of this method was described by
174 Saxton and Jacobson, 1997. Only selected tracks with a certain minimum length
175 (typically eight or more localized positions) are used for further analyses, removing
176 short track artifacts that may originate from background signals. The mean MSD over
177 all tracks is calculated and the diffusion coefficient is estimated via a linear fit
178 (Figure 2B, lower left plot) that commonly only includes the first few points of an MSD
179 curve. While this averaged analysis gives a first impression of protein mobility, a more
180 detailed analysis is possible by estimating individual diffusion coefficients for the MSD
181 curves of each track. Their distribution can then be plotted as a histogram (Figure 2B,
182 lower right plot), revealing the potential existence of nonuniform mobility distributions
183 that would remain hidden in the mean MSD plot. Due to the small number of data
184 points for individual tracks, a goodness-of-fit threshold value (the adjusted R^2) can be
185 specified for the linear fit to reject inconclusive results. In addition to storing the peak
186 log(D) value for each file examined, the relative proportion of multiple populations can
187 also be estimated. Performing the MSD analysis adds new options to the tracking
188 images, such as coloring tracks based on their mobility or splitting them visually into
189 mobile and immobile tracks (for more details refer to the user guide).

190 ***Cluster analysis***

191 While mobility analysis provides information about the dynamics of membrane
192 proteins, their spatial organization can also be obtained by cluster analysis based on
193 the single-molecule data using OneFlowTraX, which implements several current state-

194 of-the-art methods. Our analysis pipeline includes Voronoi tessellation (Andronov et
195 al., 2016; Levet et al., 2015), density-based spatial clustering of applications with noise
196 (DBSCAN) (Ester et al., 1996) and the recently introduced nanoscale spatiotemporal
197 indexing clustering (NASTIC) (Wallis et al., 2023) (Figure 3A). A detailed description
198 of these methods can also be found in the user guide.

199 When applying the different clustering methods, the user can base the analysis in
200 OneFlowTraX (Figure 3B) on two different data sets: (i) all localized fluorophore
201 positions in the sample or (ii) the centroids of the assembled tracks. Option (i)
202 disregards the assignment of localizations to individual membrane proteins, which can
203 result in varying numbers of cluster points for each protein, while option (ii) assigns
204 each detected membrane protein to one cluster point, at the expense of a smaller set
205 of points (also compare Figure 3A). This choice largely depends on the available data
206 quantity, but option (ii) should be generally preferred for its more consistent
207 assignment. Only the NASTIC method is based solely on the protein tracks
208 themselves, since their spatial overlap is used for cluster analysis. OneFlowTraX
209 implements all the above algorithms, so the users can follow their preferences or
210 compare different algorithms. The results of the applied analysis are visualized and
211 can be color-coded with different settings and exported.

212 ***Batch processing***

213 The batch analysis, outlined schematically in Figure 4A, automatically processes the
214 raw sptPALM data selected by the user and then stores all analysis results in a
215 consistent format. It allows the evaluation of big datasets, including all the above
216 analysis steps, in a very short time (about 7 seconds per file with approximately 30 000
217 localizations each). A summary of all parameters used for the individual steps in the
218 analysis of the membrane protein of interest is listed in an intuitive selection structure
219 (Figure 4B). If necessary, parameters can still be changed here, and the subsequent
220 batch analysis is performed based on these parameters collectively for all analysis
221 steps (localization, tracking, mobility and cluster analysis). The parameter list is also
222 attached to the collected results so that all steps and settings can be traced back
223 according to the FAIR principle.

Fluorophores for in planta sptPALM analysis

In plant cells, the rather impenetrable cell wall largely precludes dye- or quantum dot based single molecule tracking approaches, so that sptPALM with genetically encoded fluorescent proteins (FPs) must be used, which are fused translationally to the protein of interest. Conversely, FPs exhibit comparatively low photostability and brightness. Moreover, sptPALM analyses of proteins require photoactivatable or -convertible FP variants, where the density of visible fluorophores per image is controlled by an additional activation laser, further limiting the pool of applicable FPs. Genetic constructs encoding photoconvertible mEos2 fusions have been useful for sptPALM-based analyses of membrane proteins in plant cells (Gronnier et al, 2017; Hosy et al, 2015; Smokvarska et al, 2023). However, it was shown previously that mEos2 tends to form oligomers and aggregates in animal cells, especially when fused to membrane proteins (Zhang et al., 2012). We therefore recommend to prefer the improved version mEos3.2 that is monomeric and also works in plants (Jolivet et al, 2023). As with mEos2, the native green form of mEos3.2 can be converted to a red form using light of ~400 nm wavelength, allowing to adjust the density of the visible fluorophores in the red imaging channel. However, as mEos3.2 occupies both the green and red parts of the spectrum, it is not compatible to combine it with other FPs for potential dual-color applications. Based on their photophysical characteristics (Supplemental Table 1), we propose the use of photoactivatable (PA-) GFP (Patterson and Lippincott-Schwartz, 2002) and PATagRFP (Subach et al., 2010) as additional fluorophores for sptPALM applications in plant cells. Both PA FPs are non-fluorescent in their respective native forms and can be converted to their spectrally distinct fluorescent forms with light of ~400 nm, enabling simultaneous imaging of differently labeled proteins in two color channels. The three fluorophore coding sequences were codon-optimized for their use in plant cells (Supplemental Table 2).

Biological applications using OneFlowTraX

PM proteins used for proof-of-principle sptPALM analyses

In order to demonstrate the applicability of OneFlowTraX for sptPALM analyses with focus on plant cells, well-described *A. thaliana* membrane proteins were used, namely BRI1, RLP44, LTi6a and the aquaporin PIP2;1. LTi6a-mEos2 and PIP2;1-mEos2 *A. thaliana* transgenic lines (Hosy et al, 2015) are under the control of the *PIP2;1* promoter (*pPIP2;1*). BRI1 and RLP44 were expressed as mEos3.2, PA-GFP and

257 PATagRFP fusions under the control of the respective native promoter (*pBRI1*,
258 *pRLP44*).

259 The aquaporin PIP2;1 is a large six transmembrane domains-containing, tetrameric
260 water and hydrogen peroxide permeable pore (Dynowski et al., 2008), whereas LTi6a
261 is a small two transmembrane domains-containing intrinsic PM protein of yet unclear
262 function (Kim et al., 2021). BRI1 initiates well-understood signaling pathways in plant
263 cells. Upon binding of BR to BRI1's extracellular domain, its interaction with the co-
264 receptor BRI1-ASSOCIATED KINASE 1 (BAK1) is enhanced. This leads to a re-
265 arrangement of proteins within the complex, eventually resulting in auto- and
266 transphosphorylation of their kinase domains and its full signaling activity (Gou and Li,
267 2020; Wolf, 2020). The outcomes of BR activation of the BRI1/BAK1 complex are on
268 the one hand the differential regulation of BR-responsive genes via a nucleo-
269 cytoplasmic signaling cascade (Mora-Garcia et al., 2004; Vert and Chory, 2006; Yin et
270 al., 2005; Zhu et al., 2017) and on the other hand a rapid acidification of the apoplast
271 via the activation of PM-resident P-type proton pumps (Caesar et al., 2011; Grosseholz
272 et al., 2022; Witthöft et al., 2011)

273 RLP44 is proposed to be a cell wall integrity sensor that controls cell wall homeostasis
274 by interplay with BRI1 and BAK1 (Wolf et al., 2012; Wolf et al., 2014). In fact, we were
275 recently able to demonstrate the existence of a ternary RLP44/BRI1/BAK1 complex in
276 the PM of living plant cells using a spectral Förster resonance energy transfer (FRET)
277 and FRET-Fluorescence-lifetime imaging microscopy (FLIM) approach (Glöckner et
278 al., 2022). Additionally, RLP44 has been linked to phytosulfokine signaling. The
279 corresponding receptor Phytosulfokine Receptor 1 (PSKR1) is also proposed to form
280 a complex with RLP44 and BAK1 (Gomez et al., 2021; Holzwart et al., 2018).

281 ***OneFlowTraX analysis of BRI1 and RLP44 dynamics and nano-structured organization***
282 ***in the Nicotiana benthamiana transient expression system and transgenic Arabidopsis***
283 ***seedlings***

284 For initial assessment, mEos3.2, PA-GFP and PATagRFP-tagged BRI1 fusion proteins
285 were transiently expressed in *Nicotiana benthamiana* (*N. benthamiana*) epidermal leaf
286 cells. Such transient expression setups provide a fast and convenient way to test the
287 functionality of protein fusions with photoswitchable/photoconvertible fluorophores
288 (Gronnier et al, 2017; Perraki et al, 2018). For the transgenic approach in *A. thaliana,*
289 the mEos3.2, PA-GFP and PATagRFP-tagged fusions of RLP44 were chosen.

290 The density of the single fusion proteins after photoconversion or –activation was
291 optimal (Figure 5A) for a comprehensive evaluation of sptPALM data (Bayle et al,
292 2021).

293 Using OneFlowTraX (for detailed parameters see Supplemental Table 4), the data
294 were processed, and single-molecule trajectories were generated (Figure 5B). After
295 MSD analysis, the diffusion coefficients were calculated (Figure 5C).

296 Although the three fluorophores are sptPALM-optimized versions of different
297 precursors from various marine organisms, the BRI1 fusion proteins showed
298 comparable diffusion coefficients in *N. benthamiana* epidermal leaf cells (Figure 5C,
299 left panel). The same was observed for the RLP44 fusion proteins in transgenic
300 *Arabidopsis* epidermal hypocotyl cells (Figure 5C, right panel). This demonstrates that
301 all three fluorophores can be reliably used for sptPALM studies in different plant cell
302 systems. The best signal-to-noise ratio was obtained with mEos3.2, due to its excellent
303 photophysical properties (Supplemental Table 1). On the other hand, PA-GFP and
304 PATagRFP can be combined - due to their non-overlapping spectra - for dual-color
305 sptPALM experiments.

306 Moreover, as shown in Figure 5D, OneFlowTraX allows the use of sptPALM single-
307 molecule track data to show that the BRI1-mEos3.2 and RLP44-mEos3.2 fusion
308 proteins are partially organized in clusters.

309 ***OneFlowTraX application examples to detect changes in protein mobility***

310 To validate the usefulness of OneFlowTraX, we first analyzed the dynamics of
311 LTi6a-mEos2 and PIP2;1-mEos2 (Hosy et al, 2015) in the PM of epidermal root tip and
312 epidermal hypocotyl cells of transgenic *A. thaliana* seedlings. In accordance with their
313 previous results, we observed that LTi6a exhibited a significantly higher mobility than
314 PIP2;1 in the PM of root epidermal cells (Figure 6A, left). We found that this difference
315 was even more pronounced in the PM of epidermal hypocotyl cells (Figure 6A, right).
316 Moreover, the mobility of LTi6A was significantly higher in the PM of epidermal
317 hypocotyl cells than in epidermal cells of the root. In contrast, we observed no
318 difference for PIP2;1 (Figure 6A).

319 We then conducted OneFlowTraX analysis of the RLP44-mEos3.2 dynamics in
320 transgenic *A. thaliana* seedlings grown either in white light or darkness in order to
321 determine whether the developmental state (photomorphogenic versus

322 skotomorphogenic) influences the fusion protein's dynamics. Firstly, as shown in
323 Figure 6B, RLP44-mEos3.2 moved significantly faster in the PM of cells of the upper
324 part of dark-grown hypocotyls compared to the lower part. The diffusion coefficient of
325 RLP44-mEos3.2 in the PM of hypocotyl cells of light-grown seedlings, where a
326 differentiation of different cell types along the axis is hardly possible, was similar to the
327 diffusion coefficients gained from the lower part of the etiolated hypocotyl. These in
328 planta generated results show that positional and developmental differences in the
329 RLP44-mEos3.2 dynamics can be detected by sptPALM-based OneFlowTraX
330 analysis.

331 The effect of other environmental factors on protein mobility can also be evaluated by
332 OneFlowTraX. Here we chose the hyper-osmotic stress response of plant cells after
333 addition of sorbitol, a non-toxic, widely used, non-metabolic osmolyte already applied
334 for sptPALM (Hosy et al, 2015). Sorbitol induces a cell volume loss (plasmolysis) when
335 used at a concentration of 300 mM. Under milder hyper-osmotic conditions (100 mM),
336 the cells experience a reduction in turgor without major changes in their volume
337 (Martiniere et al., 2019). Thus, the increasing concentration of sorbitol from 100 to
338 300 mM induces a progressive separation of the PM from the cell wall which enhanced
339 the dynamics of almost all intrinsic PM proteins (Hosy et al, 2015). Based on this
340 knowledge, treatments with 100 mM and 300 mM sorbitol or mock treatment (all
341 applied for 20 min) were performed with light-grown and dark-grown seedlings
342 expressing RLP44-mEos3.2. Then, the sptPALM data were measured in epidermal
343 hypocotyl cells of light-grown seedlings and epidermal cells of the upper hypocotyl part
344 of dark-grown seedlings and analyzed using OneFlowTraX. Whereas the
345 concentration of 100 mM sorbitol did not significantly affect the diffusion coefficient of
346 RLP44-mEos3.2 compared to the mock treatment (0 mM), 300 mM sorbitol
347 significantly increased the protein mobility in all measured cells (Figure 6C).

348 These examples represent common analyses of sptPALM data in plant research and
349 demonstrate the applicability of OneFlowTraX, which was used to perform all analysis
350 steps, including localization, tracking and protein mobility analysis.

351 # DISCUSSION

352 ## OneFlowTraX is an all-in-one software package for SMLM data processing
353 and analysis.

354 With OneFlowTraX, we provide a unique, user-friendly open-source software package
355 that guides users through the steps of localization, tracking, analysis of mobility and
356 nanoscale organization of single molecules based on SMLM data. OneFlowTraX
357 facilitates the previously very time-consuming and cumbersome post-acquisition
358 processing of SMLM data. Although OneFlowTraX is tailored for use by cell biologists,
359 who want to perform sptPALM analyses in the PM of plant cells, it also opens the
360 possibility to post-acquisition data processing for other non-PM bound processes in
361 any prokaryotic and eukaryotic cells. For instance, the software could be used to
362 analyze the spatial organization of chromosomes into topologically associating
363 domains (Wang et al., 2016).

364 In plants, due to the cell wall, only regions close to the microscope slide can be
365 analyzed such as the PM and PM-associated molecules. OneFlowTraX provides a
366 default set of analysis parameters that are well suited for plant PM molecules located
367 in a 2D environment.

368 However, as described in the provided manual, all settings can be adjusted by the
369 users to their specific experimental requirements for the SMLM analysis of any
370 process of interest independent of the organism. Moreover, the batch processing with
371 detailed parameter and data output is available for all analysis paths, maintaining the
372 consistency of the sptPALM data with the calculated results. The detailed but clearly
373 structured parameter organization also allows to investigate the influence of individual
374 parameters in the overall analysis process on the results, providing a method to
375 evaluate the reliability of the analyses. Importantly, the data management procedure
376 of OneFlowTraX follows the FAIR guiding principles for scientific data management
377 and stewardship. Due to its open-source characteristics, OneFlowTraX also allows
378 users to customize or extend the program according to their needs.

379 OneFlowTraX was programmed in MATLAB, a software language that is easy to work
380 with and widely used in academia. Care was taken to make the code straightforward
381 to understand and all programming steps are commented to make it easier to insert

382 changes or add extensions, which could also make OneFlowTraX interesting for
383 scientists working with animal or human cell cultures.

384 PATagRFP, PA-GFP and mEos3.2 are suitable FPs for sptPALM analyses
385 in living plant cells

386 Especially plant scientists rely on genetically encoded photoactivatable or
387 photoconvertible FPs fused to the protein of interest as the cell wall is impenetrable
388 for dyes applied from the outside. With mEos3.2, PA-GFP and PATagRFP, three
389 different FPs are now available that do not tend to aggregate, deliver satisfactory
390 signal-to-noise ratios during imaging and are therefore applicable for sptPALM
391 applications both in a transient transformation system (*N. benthamiana*) and in stably
392 transformed *A. thaliana* plants. We expect that these fluorophores will also work in
393 other plant species. Of particular interest is the combination of PA-GFP and
394 PATagRFP, which will enable dual-color sptPALM in the future for simultaneous
395 recording and spatiotemporal analysis of two different fusion proteins. Because of its
396 superior photophysical properties, we recommend the use of mEos3.2 for single FP
397 fusion protein analyses. Especially when analyzing the mobility of PM proteins in living
398 plant cells, the sptPALM technology shows its superiority in terms of spatiotemporal
399 resolution compared with other methods such as FRAP and FCS (Bayle et al, 2021).

400 OneFlowTraX allows the rapid in vivo analysis of PM proteins in
401 transiently and stably transformed plant cells

402 We used two functionally well-studied PM proteins, namely BRI1 and RLP44, for our
403 proof-of-principle experiments regarding the usability of the three FPs and the
404 applicability of OneFlowTraX. Both proteins were evaluated in either transiently
405 transformed *N. benthamiana* epidermal leaf cells or the epidermis of the hypocotyl of
406 stable transgenic *A. thaliana* seedlings. Importantly, the accumulation of the BRI1 and
407 RLP44 fusion proteins was driven by the respective endogenous promoters. Our
408 experience has been that strong over-accumulation of the fusion proteins driven by
409 constitutively active promoters leads to overcrowded sptPALM movies in both plant
410 systems. Analysis of these movies results in misconnected tracks that affect the entire
411 OneFlowTraX analysis causing inadequate results in subsequent steps. Therefore, we
412 recommend using weaker promoters whenever possible.

413 While OneFlowTraX further demonstrated its utility through the replication of LTi6a-
414 mEos2 and PIP2;1-mEos2 sptPALM-derived findings in the roots of light-grown
415 *A. thaliana* seedlings (Hosy et al, 2015), we were additionally able to observe that the
416 PM dynamics of both mEos2 fusions differ between epidermal cells of the root and
417 hypocotyl. This suggests that the organ context of a tissue has an influence on PM
418 protein dynamics in plant cells.

419 Moreover, during our OneFlowTraX analysis of the RLP44-mEos3.2 dynamics in
420 epidermal cells of light-grown *Arabidopsis* hypocotyls, we observed high data
421 variability. This led to the hypothesis that cell-specific effects depending on the cell's
422 position in the organ, i.e., on its physiological state, interfere with the membrane
423 dynamics of the fusion protein to be investigated. This hypothesis was substantiated
424 by the technically easier access to the potential positional effects in the dynamics of
425 RLP44-mEos3.2 in epidermal cells along the hypocotyl axis of dark-grown seedlings:
426 The diffusion coefficient of RLP44-mEos3.2 is significantly higher in the epidermal cells
427 of the upper part than in those of the lower part of the dark-grown hypocotyl.
428 Furthermore, the diffusion coefficient in the lower part is similar to that found in the
429 epidermal cells of light-grown hypocotyls. Thus, OneFlowTraX can easily capture
430 differences in dynamics, allowing SMLM in different cells and tissues that may vary in
431 their membrane properties.

432 As previously shown by Hosy et al, 2015 and Martiniere et al, 2019, the treatment of
433 *A. thaliana* root cells with increasing concentration of the osmolyte sorbitol increases
434 the diffusion coefficient of membrane proteins such as the aquaporin PIP2;1. Using
435 OneFlowTraX, we could substantiate these findings for the RLP44-mEos3.2 fusion
436 and demonstrated potential effects of the differentiation states of the analyzed tissue.
437 This shows that reproducible and robust SMLM data analysis is provided by
438 OneFlowTraX.

439 In addition to the analysis of protein dynamics, OneFlowTraX also offers different
440 algorithms (Voronoi tessellation, DBSCAN, NASTIC) for the analysis of the nanoscale
441 organization of a given membrane protein. For sptPALM data, we recommend the
442 NASTIC algorithm as it is specifically designed to work with track data. Because of the
443 sensitivity to parameter changes, care must be taken when regarding the results of
444 the nanoscale evaluation output by all of these algorithms as absolute values.
445 However, relative comparisons of the nanoscale organization for a given membrane

446 protein are possible if there are no changes in the parameter settings between the
447 experiments.

448 In summary, SMLM data acquisition such as that from sptPALM becomes more easily
449 accessible and faster analyzable with OneFlowTraX. The fluorophores mEos3.2, PA-
450 GFP and PATagRFP have proven to be suitable for SMLM in planta and allow analysis
451 of membrane proteins in transient expression systems as well as in stable transformed
452 plants. The respective FP fusions are suitable for the analysis of protein dynamics in
453 epidermal cells of different organs and at different developmental or physiological
454 stages as well as in response to environmental factors. Therefore, OneFlowTraX will
455 greatly facilitate the comprehensive investigation of the dynamics and nanoscale
456 organization of single molecules in the future.

457 # METHODS

458 ## Plasmid construction

459 All expression clones were constructed using GoldenGate assembly with BB10 as the
460 vector (Binder et al., 2014). Promoter sequences were obtained with the help of the
461 Integrated Genome Browser (Freese et al., 2016). Level I modules were generated by
462 PCR amplification of the desired sequences and then blunt-end cloned into pJET1.2
463 (Thermo Fisher Scientific). Fluorophores were designed as C-terminal fusions
464 (D-E module) using either a glycine/serine or a glycine/alanine-rich linker. The coding
465 sequences of BRI1 and RLP44 were constructed as B-D modules, eliminating the
466 need for a B-C dummy module. A full list of used constructs can be found in
467 Supplemental Table 5. The correctness of Level I constructs was confirmed by Sanger
468 sequencing. Cut-ligations for the Level II generation were performed with 40 cycles,
469 without using bovine serum albumin as described by Binder et al, 2014. Reactions
470 were transformed into TOP10 cells (Thermo Fisher Scientific), and colony correctness
471 was verified via restriction enzyme analysis and partial Sanger sequencing.

472 ## Plant material and growth conditions

473 The transgenic *A. thaliana* lines generated for this study were all in the Columbia
474 (Col-0) background. The respective stable lines were created using the Floral dip
475 method according to Zhang et al., 2006. For the reproduction of LTi6a and PIP2;1

476 results, seeds of the corresponding lines were provided by Dr. Doan-Trung Luu.
477 Transgenic seeds were propagated either based on the presence of the pFAST marker
478 by binocular visual inspection or by selection of survivors on ½ Murashige and Skoog
479 (MS) plates containing 1 % (w/v) sucrose and 0.8 % (w/v) phytoagar supplemented
480 with 25 µM hygromycin. For sptPALM measurements, seeds were sterilized with a
481 solution of 70 % ethanol (v/v) and 0.05 % Triton X-100 for 30 minutes followed by a
482 10-minute treatment with absolute ethanol. Seeds were sown on ½ MS plates (+1 %
483 sucrose and 0.8 % phytoagar) and stratified at 4 °C for at least 24 hours. For
484 measurements of dark-grown seedlings, seeds were exposed to light from the growth
485 chamber for two hours before being wrapped in aluminum foil until the day of
486 measurement. Light-grown seedlings were cultivated in growth chambers at 20 °C
487 under long-day conditions (16 hours light / 8 hours dark). The duration of growth is
488 indicated in the respective figures. The *N. benthamiana* plants used in this study were
489 cultivated under controlled greenhouse conditions. Proteins were transiently
490 expressed using the AGL1 *Agrobacterium tumefaciens* strain (Lifeasible), as
491 previously described (Hecker et al., 2015; Ladwig et al., 2015), without the washing
492 step with sterile water. The plants were infiltrated with the respective construct at an
493 OD600 of 0.1, in a ratio of 1:1 with the silencing inhibitor p19. After watering, the plants
494 were kept in ambient conditions and were imaged three days after infiltration.

495 **Sample preparation and movie acquisition**

496 All sptPALM measurements with transiently transformed *N. benthamiana* were
497 performed three days after infiltration. A small leaf area was cut out, excluding veins,
498 and placed between two coverslips (Epredia 24x50 mm #1 or equivalent) with a drop
499 of water. This “coverslip sandwich” was then placed on the specimen stage, lightly
500 weighted down by a brass ring to help flatten the uneven cell layers, especially in
501 *N. benthamiana*. Seven-day-old *A. thaliana* seedlings were used to acquire data from
502 stable *Arabidopsis* lines. Depending on the experiment, either light-grown or dark-
503 grown plants were used. For sorbitol (obtained by Roth) treatments, seedlings were
504 incubated with the appropriate concentration in 12-well plates for five minutes before
505 being transferred to the coverslip and imaged in the respective incubation solution as
506 mounting medium for up to 20 minutes. Similar to the handling of *N. benthamiana* leaf
507 discs, the seedlings were placed between coverslips and brass rings.

508 The custom-built microscope platform for sptPALM acquisition is described in detail in
509 Supplementary Materials and Methods. Briefly, lasers of different wavelengths and
510 their intensities are controlled by an acousto-optic transmission filter. A laterally
511 translatable lens in the excitation beam path allows to adjust the VAEM illumination of
512 the sample utilizing a high NA objective. The emitted light from the sample is separated
513 from the excitation light by a multi-band beam splitter and is detected by an sCMOS
514 camera. Depending on the fluorophore fusion, the following filters were inserted into
515 the emission beam path: (i) mEos3.2: 568 LP Edge Basic Longpass Filter, 584/40 ET
516 Bandpass; (ii) PA-GFP: 488 LP Edge Basic Longpass Filter, 525/50 BrightLine HC;
517 (iii) PATagRFP: 568 LP Edge Basic Longpass Filter, 600/52 BrightLine HC (all AHF
518 analysentechnik AG). The excitation power arriving at the sample was measured
519 (PM100D with S120C, Thorlabs) in epifluorescence mode after the objective to keep
520 it constant for the respective experiment sets. If necessary, photoconversion or
521 photoactivation was performed using 405 nm excitation at varying low intensities (for
522 detailed acquisition parameters see Supplemental Table 4). The magnification of the
523 optical system was adjusted so that the length of one camera pixel corresponds to
524 100 nm in the sample plane. Viable regions of interest were screened in a larger area
525 of 51.2 x 51.2 µm by adjusting the focal plane and the VAEM angle with a frame rate
526 of 10 Hz, while recording was performed with 12.8 x 12.8 µm and frame rates between
527 20 and 50 Hz, recording between 2 500 and 5 000 frames per movie (see
528 Supplemental Table 4). For each measurement day, noise files (a series of dark
529 images) were recorded with the corresponding frame rates.

530 **Raw data processing and analysis with OneFlowTraX**

531 Subsets of each experimental data set were loaded into OneFlowTraX to inspect the
532 quality of the data and to find appropriate parameters for each analysis step as
533 described above. On the Batch Analysis tab, all sptPALM raw data files that share the
534 same parameter set were processed together (see Supplemental Table 4 for a detailed
535 list of applied analysis parameters). Samples that showed significantly low numbers
536 of localizations or tracks compared to others in the same batch were discarded.

537 SUPPLEMENTAL INFORMATION

538 Document S1. Supplemental information.

FUNDING

Our research was supported by the German Research Foundation (DFG) via the CRC 1101 to A.J.M., B.K., J.G., K.H. and S.z.O.-K., and by individual DFG grants to K.H. (HA 2146/22, HA 2146/23). We also thank the DFG for grants for scientific equipment (FUGG: INST 37/991-1, INST 37/992-1, INST 37/819-1, INST 37/965-1).

AUTHOR CONTRIBUTIONS

Conceptualization, A.J.M., B.K., K.H., and S.z.O.-K.; Software, S.z.O.-K.; Formal Analysis, L.R. and S.z.O.-K.; Data Curation, L.R., LI.R., and S.z.O.-K.; Methodology, S.z.O.-K.; Investigation, L.R., LI.R., and S.z.O.-K.; Writing – Original Draft, K.H., L.R., and S.z.O.-K.; Writing – Review & Editing, A.J.M., B.K., K.H., J.G., L.R., LI.R., and S.z.O.-K.; Visualization, L.R. and S.z.O.-K.; Funding Acquisition, A.J.M., B.K., and K.H.; Resources, A.E., A.J.M., and N.G.B.; Supervision, A.J.M., J.G., B.K., and K.H.

DATA AND SOFTWARE AVAILABILITY

The OneFlowTraX software (including a user guide), is freely available to non-commercial users at GitHub (https://github.com/svenzok/OneFlowTraX).

ACKNOWLEDGMENTS

We would like to thank Dr. Andrea Gust for providing us with the pFAST construct. We would also like to thank Dr. Doan-Trung Luu for providing seeds of the LTi6a-mEos2 and PIP2;1-mEos2 transgenic *A. thaliana* lines. No conflict of interest is declared.

REFERENCES

Andronov, L., Orlov, I., Lutz, Y., Vonesch, J.L., and Klaholz, B.P. (2016). ClusterViSu, a method for clustering of protein complexes by Voronoi tessellation in super-resolution microscopy. Sci. Rep. **6**:24084. https://doi.org/10.1038/srep24084.

Axelrod, D., Koppel, D.E., Schlessinger, J., Elson, E., and Webb, W.W. (1976). Mobility Measurement by Analysis of Fluorescence Photobleaching Recovery Kinetics. Biophys. J. **16**:1055-1069. https://doi.org/10.1016/S0006-3495(76)85755-4.

Bayle, V., Fiche, J.B., Burny, C., Platre, M.P., Nollmann, M., Martiniere, A., and Jaillais, Y. (2021). Single-particle tracking photoactivated localization microscopy of

567 membrane proteins in living plant tissues. Nat. Protoc. **16**:1600-1628.
568 https://doi.org/10.1038/s41596-020-00471-4.

569 **Betzig, E., Patterson, G.H., Sougrat, R., Lindwasser, O.W., Olenych, S.,**
570 **Bonifacino, J.S., Davidson, M.W., Lippincott-Schwartz, J., and Hess, H.F.** (2006).
571 Imaging intracellular fluorescent proteins at nanometer resolution. Science **313**:1642-
572 1645. https://doi.org/10.1126/science.1127344.

573 **Binder, A., Lambert, J., Morbitzer, R., Popp, C., Ott, T., Lahaye, T., and Parniske,**
574 **M.** (2014). A modular plasmid assembly kit for multigene expression, gene silencing
575 and silencing rescue in plants. PLoS One **9**:e88218.
576 https://doi.org/10.1371/journal.pone.0088218.

577 **Caesar, K., Elgass, K., Chen, Z., Huppenberger, P., Witthoft, J., Schleifenbaum,**
578 **F., Blatt, M.R., Oecking, C., and Harter, K.** (2011). A fast brassinolide-regulated
579 response pathway in the plasma membrane of Arabidopsis thaliana. Plant J. **66**:528-
580 540. https://doi.org/10.1111/j.1365-313X.2011.04510.x.

581 **Chenouard, N., Smal, I., de Chaumont, F., Maska, M., Sbalzarini, I.F., Gong, Y.H.,**
582 **Cardinale, J., Carthel, C., Coraluppi, S., Winter, M., et al.** (2014). Objective
583 comparison of particle tracking methods. Nat. Methods **11**:281-289.
584 https://doi.org/10.1038/nmeth.2808.

585 **Dynowski, M., Schaaf, G., Loque, D., Moran, O., and Ludewig, U.** (2008). Plant
586 plasma membrane water channels conduct the signalling molecule H2O2. Biochem.
587 J. **414**:53-61. https://doi.org/10.1042/Bj20080287.

588 **Ester, M., Kriegel, H.-P., Sander, J., and Xu, X.** (1996). A density-based algorithm for
589 discovering clusters in large spatial databases with noise. Proceedings of the Second
590 International Conference on Knowledge Discovery and Data Mining:226–231.

591 **Freese, N.H., Norris, D.C., and Loraine, A.E.** (2016). Integrated genome browser:
592 visual analytics platform for genomics. Bioinformatics **32**:2089-2095.
593 https://doi.org/10.1093/bioinformatics/btw069.

594 **Glöckner, N., zur Oven-Krockhaus, S., Rohr, L., Wackenhut, F., Burmeister, M.,**
595 **Wanke, F., Holzwart, E., Meixner, A.J., Wolf, S., and Harter, K.** (2022). Three-
596 Fluorophore FRET Enables the Analysis of Ternary Protein Association in Living Plant
597 Cells. Plants **11**:2630. https://doi.org/10.3390/plants11192630.

598 **Gomez, B.G., Holzwart, E., Shi, C., Lozano-Duran, R., and Wolf, S.** (2021).
599 Phosphorylation-dependent routing of RLP44 towards brassinosteroid or

600 phytosulfokine signalling. J. Cell Sci. **134**:jcs259134.
601 https://doi.org/10.1242/jcs.259134.

602 **Gou, X., and Li, J.** (2020). Paired Receptor and Coreceptor Kinases Perceive
603 Extracellular Signals to Control Plant Development. Plant Physiol. **182**:1667-1681.
604 https://doi.org/10.1104/pp.19.01343.

605 **Gronnier, J., Legrand, A., Loquet, A., Habenstein, B., Germain, V., and Mongrand,**
606 **S.** (2019). Mechanisms governing subcompartmentalization of biological membranes.
607 Curr. Opin. Plant Biol. **52**:114-123. https://doi.org/10.1016/j.pbi.2019.08.003.

608 **Gronnier, J., Crowet, J.M., Habenstein, B., Nasir, M.N., Bayle, V., Hosy, E., Platre,**
609 **M.P., Gouguet, P., Raffaele, S., Martinez, D., et al.** (2017). Structural basis for plant
610 plasma membrane protein dynamics and organization into functional nanodomains.
611 eLife **6**:e26404. https://doi.org/10.7554/eLife.26404.

612 **Grosseholz, R., Wanke, F., Rohr, L., Glöckner, N., Rausch, L., Scholl, S., Scacchi,**
613 **E., Spazierer, A.J., Shabala, L., Shabala, S., et al.** (2022). Computational modeling
614 and quantitative physiology reveal central parameters for brassinosteroid-regulated
615 early cell physiological processes linked to elongation growth of the Arabidopsis root.
616 eLife **11**:73031. https://doi.org/10.7554/eLife.73031.

617 **Hecker, A., Brand, L.H., Peter, S., Simoncello, N., Kilian, J., Harter, K., Gaudin, V.,**
618 **and Wanke, D.** (2015). The Arabidopsis GAGA-Binding Factor BASIC
619 PENTACYSTEINE6 Recruits the POLYCOMB-REPRESSIVE COMPLEX1
620 Component LIKE HETEROCHROMATIN PROTEIN1 to GAGA DNA Motifs. Plant
621 Physiol. **168**:1013-1024. https://doi.org/10.1104/pp.15.00409.

622 **Hess, S.T., Girirajan, T.P.K., and Mason, M.D.** (2006). Ultra-high resolution imaging
623 by fluorescence photoactivation localization microscopy. Biophys. J. **91**:4258-4272.
624 https://doi.org/10.1529/biophysj.106.091116.

625 **Holzwart, E., Huerta, A.I., Glockner, N., Garnelo Gomez, B., Wanke, F., Augustin,**
626 **S., Askani, J.C., Schurholz, A.K., Harter, K., and Wolf, S.** (2018). BRI1 controls
627 vascular cell fate in the Arabidopsis root through RLP44 and phytosulfokine signaling.
628 Proc. Natl. Acad. Sci. U.S.A. **115**:11838-11843.
629 https://doi.org/10.1073/pnas.1814434115.

630 **Hosy, E., Martiniere, A., Choquet, D., Maurel, C., and Luu, D.T.** (2015). Super-
631 resolved and dynamic imaging of membrane proteins in plant cells reveal contrasting
632 kinetic profiles and multiple confinement mechanisms. Mol. Plant **8**:339-342.
633 https://doi.org/10.1016/j.molp.2014.10.006.

Jaillais, Y., and Ott, T. (2020). The Nanoscale Organization of the Plasma Membrane and Its Importance in Signaling: A Proteolipid Perspective(1)([OPEN]). Plant Physiol. **182**:1682-1696. https://doi.org/10.1104/pp.19.01349.

Jaqaman, K., Loerke, D., Mettlen, M., Kuwata, H., Grinstein, S., Schmid, S.L., and Danuser, G. (2008). Robust single-particle tracking in live-cell time-lapse sequences. Nat. Methods **5**:695-702. https://doi.org/10.1038/nmeth.1237.

Jolivet, M.D., Deroubaix, A.F., Boudsocq, M., Abel, N.B., Rocher, M., Robbe, T., Wattelet, V., Huard, J., Lefebvre, D., Lu, Y.L., et al. (2023). Interdependence of a kinase and its cognate substrate plasma membrane nanoscale dynamics underlies Arabidopsis response to viral infection. bioRxiv:2023.2007.2031.551174. https://doi.org/10.1101/2023.07.31.551174.

Kim, H.S., Park, W., Lee, H.S., Shin, J.H., and Ahn, S.J. (2021). Subcellular Journey of Rare Cold Inducible 2 Protein in Plant Under Stressful Condition. Front. Plant Sci. **11**:610251. https://doi.org/10.3389/fpls.2020.610251.

Konopka, C.A., and Bednarek, S.Y. (2008). Variable-angle epifluorescence microscopy: a new way to look at protein dynamics in the plant cell cortex. Plant J. **53**:186-196. https://doi.org/10.1111/j.1365-313X.2007.03306.x.

Ladwig, F., Dahlke, R.I., Stuhrwohldt, N., Hartmann, J., Harter, K., and Sauter, M. (2015). Phytosulfokine Regulates Growth in Arabidopsis through a Response Module at the Plasma Membrane That Includes CYCLIC NUCLEOTIDE-GATED CHANNEL17, H+-ATPase, and BAK1. Plant Cell **27**:1718-1729. https://doi.org/10.1105/tpc.15.00306.

Lelek, M., Gyparaki, M.T., Beliu, G., Schueder, F., Griffie, J., Manley, S., Jungmann, R., Sauer, M., Lakadamyali, M., and Zimmer, C. (2022). Single-molecule localization microscopy (vol 1, 39, 2021). Nat. Rev. Methods Primers **2**https://doi.org/10.1038/s43586-022-00161-3.

Levet, F., Hosy, E., Kechkar, A., Butler, C., Beghin, A., Choquet, D., and Sibarita, J.B. (2015). SR-Tesseler: a method to segment and quantify localization-based super-resolution microscopy data. Nat. Methods **12**:1065-1071. https://doi.org/10.1038/nmeth.3579.

Magde, D., Webb, W.W., and Elson, E. (1972). Thermodynamic Fluctuations in a Reacting System - Measurement by Fluorescence Correlation Spectroscopy. Phys. Rev. Lett. **29**:705-708. https://doi.org/10.1103/PhysRevLett.29.705.

667 **Manley, S., Gillette, J.M., Patterson, G.H., Shroff, H., Hess, H.F., Betzig, E., and**
668 **Lippincott-Schwartz, J.** (2008). High-density mapping of single-molecule trajectories
669 with photoactivated localization microscopy. Nat. Methods **5**:155-157.
670 https://doi.org/10.1038/Nmeth.1176.

671 **Manzo, C., and Garcia-Parajo, M.F.** (2015). A review of progress in single particle
672 tracking: from methods to biophysical insights. Rep. Prog. Phys. **78**:124601.
673 https://doi.org/10.1088/0034-4885/78/12/124601.

674 **Martiniere, A., and Zelazny, E.** (2021). Membrane nanodomains and transport
675 functions in plant. Plant Physiol. **187**:1839-1855.
676 https://doi.org/10.1093/plphys/kiab312.

677 **Martiniere, A., Fiche, J.B., Smokvarska, M., Mari, S., Alcon, C., Dumont, X.,**
678 **Hematy, K., Jaillais, Y., Nollmann, M., and Maurel, C.** (2019). Osmotic Stress
679 Activates Two Reactive Oxygen Species Pathways with Distinct Effects on Protein
680 Nanodomains and Diffusion. Plant Physiol. **179**:1581-1593.
681 https://doi.org/10.1104/pp.18.01065.

682 **McKenna, J.F., Rolfe, D.J., Webb, S.E.D., Tolmie, A.F., Botchway, S.W., Martin-**
683 **Fernandez, M.L., Hawes, C., and Runions, J.** (2019). The cell wall regulates
684 dynamics and size of plasma-membrane nanodomains in Arabidopsis. Proc. Natl.
685 Acad. Sci. U.S.A. **116**:12857-12862. https://doi.org/10.1073/pnas.1819077116.

686 **Mora-Garcia, S., Vert, G., Yin, Y., Cano-Delgado, A., Cheong, H., and Chory, J.**
687 (2004). Nuclear protein phosphatases with Kelch-repeat domains modulate the
688 response to brassinosteroids in Arabidopsis. Genes Dev. **18**:448-460.
689 https://doi.org/10.1101/gad.1174204.

690 **Patterson, G.H., and Lippincott-Schwartz, J.** (2002). A photoactivatable GFP for
691 selective photolabeling of proteins and cells. Science **297**:1873-1877.
692 https://doi.org/10.1126/science.1074952.

693 **Perraki, A., Gronnier, J., Gouguet, P., Boudsocq, M., Deroubaix, A.F., Simon, V.,**
694 **German-Retana, S., Legrand, A., Habenstein, B., Zipfel, C., et al.** (2018). REM1.3's
695 phospho-status defines its plasma membrane nanodomain organization and activity
696 in restricting PVX cell-to-cell movement. PLoS Pathog. **14**:e1007378.
697 https://doi.org/10.1371/journal.ppat.1007378.

698 **Peters, R., Peters, J., and Tews, K.H.** (1974). Microfluorimetric Studies on
699 Translational Diffusion of Proteins in Erythrocyte-Membrane. Pflugers Arch. - Eur. J.
700 Physiol. **347**:R36-R36.

Qian, H., Sheetz, M.P., and Elson, E.L. (1991). Single-Particle Tracking - Analysis of Diffusion and Flow in 2-Dimensional Systems. Biophys. J. **60**:910-921. https://doi.org/10.1016/S0006-3495(91)82125-7.

Ries, J. (2020). SMAP: a modular super-resolution microscopy analysis platform for SMLM data. Nat. Methods **17**:870-872. https://doi.org/10.1038/s41592-020-0938-1.

Sage, D., Pham, T.A., Babcock, H., Lukes, T., Pengo, T., Chao, J., Velmurugan, R., Herbert, A., Agrawal, A., Colabrese, S., et al. (2019). Super-resolution fight club: assessment of 2D and 3D single-molecule localization microscopy software (vol 16, pg 387, 2019). Nat. Methods **16**:387-395. https://doi.org/10.1038/s41592-019-0364-4.

Saxton, M.J., and Jacobson, K. (1997). Single-particle tracking: Applications to membrane dynamics. Annu. Rev. Biophys. Biomol. Struct. **26**:373-399. https://doi.org/10.1146/annurev.biophys.26.1.373.

Smokvarska, M., Bayle, V., Maneta-Peyret, L., Fouillen, L., Poitout, A., Dongois, A., Fiche, J.B., Gronnier, J., Garcia, J., Hofte, H., et al. (2023). The receptor kinase FERONIA regulates phosphatidylserine localization at the cell surface to modulate ROP signaling. Sci. Adv. **9**:eadd4791. https://doi.org/10.1126/sciadv.add4791.

Subach, F.V., Patterson, G.H., Renz, M., Lippincott-Schwartz, J., and Verkhusha, V.V. (2010). Bright Monomeric Photoactivatable Red Fluorescent Protein for Two-Color Super-Resolution sptPALM of Live Cells. J. Am. Chem. Soc. **132**:6481-6491. https://doi.org/10.1021/ja100906g.

Tinevez, J.-Y. (2011). simpletracker. https://github.com/tinevez/simpletracker.

Tinevez, J.Y., Perry, N., Schindelin, J., Hoopes, G.M., Reynolds, G.D., Laplantine, E., Bednarek, S.Y., Shorte, S.L., and Eliceiri, K.W. (2017). TrackMate: An open and extensible platform for single-particle tracking. Methods **115**:80-90. https://doi.org/10.1016/j.ymeth.2016.09.016.

Tokunaga, M., Imamoto, N., and Sakata-Sogawa, K. (2008). Highly inclined thin illumination enables clear single-molecule imaging in cells (vol 5, pg 159, 2008). Nat. Methods **5**:455-455. https://doi.org/10.1038/nmeth0508-455.

Vert, G., and Chory, J. (2006). Downstream nuclear events in brassinosteroid signalling. Nature **441**:96-100. https://doi.org/10.1038/nature04681.

Wallis, T.P., Jiang, A., Young, K., Hou, H., Kudo, K., McCann, A.J., Durisic, N., Joensuu, M., Oelz, D., Nguyen, H., et al. (2023). Super-resolved trajectory-derived

733 nanoclustering analysis using spatiotemporal indexing. Nat. Commun. **14**:3353.
734 https://doi.org/10.1038/s41467-023-38866-y.

735 **Wang, S.Y., Su, J.H., Beliveau, B.J., Bintu, B., Moffitt, J.R., Wu, C.T., and Zhuang,**
736 **X.W.** (2016). Spatial organization of chromatin domains and compartments in single
737 chromosomes. Science **353**:598-602. https://doi.org/10.1126/science.aaf8084.

738 **Wilkinson, M.D., Dumontier, M., Aalbersberg, I.J., Appleton, G., Axton, M., Baak,**
739 **A., Blomberg, N., Boiten, J.W., Santos, L.B.D., Bourne, P.E., et al.** (2016).
740 Comment: The FAIR Guiding Principles for scientific data management and
741 stewardship. Sci. Data **3**:160018. https://doi.org/10.1038/sdata.2016.18.

742 **Witthöft, J., Caesar, K., Elgass, K., Huppenberger, P., Kilian, J., Schleifenbaum,**
743 **F., Oecking, C., and Harter, K.** (2011). The activation of the Arabidopsis P-ATPase 1
744 by the brassinosteroid receptor BRI1 is independent of threonine 948 phosphorylation.
745 Plant Signaling Behav. **6**:1063-1066. https://doi.org/10.4161/psb.6.7.15650.

746 **Wolf, S.** (2020). Deviating from the Beaten Track: New Twists in Brassinosteroid
747 Receptor Function. Int. J. Mol. Sci. **21**:1561. https://doi.org/10.3390/ijms21051561.

748 **Wolf, S., Mravec, J., Greiner, S., Mouille, G., and Hofte, H.** (2012). Plant cell wall
749 homeostasis is mediated by brassinosteroid feedback signaling. Curr. Biol. **22**:1732-
750 1737. https://doi.org/10.1016/j.cub.2012.07.036.

751 **Wolf, S., van der Does, D., Ladwig, F., Sticht, C., Kolbeck, A., Schurholz, A.K.,**
752 **Augustin, S., Keinath, N., Rausch, T., Greiner, S., et al.** (2014). A receptor-like
753 protein mediates the response to pectin modification by activating brassinosteroid
754 signaling. Proc. Natl. Acad. Sci. U.S.A. **111**:15261-15266.
755 https://doi.org/10.1073/pnas.1322979111.

756 **Yin, Y., Vafeados, D., Tao, Y., Yoshida, S., Asami, T., and Chory, J.** (2005). A new
757 class of transcription factors mediates brassinosteroid-regulated gene expression in
758 Arabidopsis. Cell **120**:249-259. https://doi.org/10.1016/j.cell.2004.11.044.

759 **Zhang, M.S., Chang, H., Zhang, Y.D., Yu, J.W., Wu, L.J., Ji, W., Chen, J.J., Liu, B.,**
760 **Lu, J.Z., Liu, Y.F., et al.** (2012). Rational design of true monomeric and bright
761 photoactivatable fluorescent proteins. Nat. Methods **9**:727-729.
762 https://doi.org/10.1038/Nmeth.2021.

763 **Zhang, X., Henriques, R., Lin, S.S., Niu, Q.W., and Chua, N.H.** (2006).
764 Agrobacterium-mediated transformation of Arabidopsis thaliana using the floral dip
765 method. Nat. Protoc. **1**:641-646. https://doi.org/10.1038/nprot.2006.97.

766 **Zhu, J.Y., Li, Y., Cao, D.M., Yang, H., Oh, E., Bi, Y., Zhu, S., and Wang, Z.Y.** (2017).
767 The F-box Protein KIB1 Mediates Brassinosteroid-Induced Inactivation and
768 Degradation of GSK3-like Kinases in Arabidopsis. Mol. Cell **66**:648-657 e644.
769 https://doi.org/10.1016/j.molcel.2017.05.012.

770

771 **Figure 1. Single-molecule localization procedure.**

772 **(A)** Single frame of a typical sptPALM image stack. Scale bar = 2 µm. **(B)** Localization
773 process. Each putative single molecule position is cut out as a larger section and fitted
774 with a two-dimensional Gaussian function. The fitting results (most importantly, the
775 coordinates) for each detected single molecule are stored as lists. **(C)** Graphical user
776 interface (GUI) of OneFlowTraX for the localization step. After loading in the sptPALM
777 files (1), the localization procedure is executed based on user-defined parameters (2),
778 with its results visualized as three histograms (PSF sizes (3), photon numbers (4) and
779 localization precision (5)) for all detected and fitted fluorescence spots. This serves as
780 quality control and allows the user to filter out, e.g., badly localized single-molecule
781 positions.

782 **Figure 2. Tracking procedure and mobility analysis.**

783 **(A)** Schematic overview of the tracking procedure and subsequent analyses. Single-
784 molecule positions are connected to trajectories when they do not exceed a maximum
785 distance (dashed circles) in subsequent frames. The Linear Assignment Problem
786 (LAP) tracker uses a global optimization and can also deal with detection gaps. All
787 tracks then undergo mean square displacement (MSD) analysis based on averaged
788 traveled distances for certain time intervals, offering mobility metrics like diffusion
789 coefficients and more extensive evaluations such as population analyses. **(B)** GUI of
790 OneFlowTraX for the tracking step, including mobility analysis. The track building
791 algorithm uses the specified parameters (6) to connect the detected localization to
792 trajectories, which are displayed in the overview image (7) and a user-defined
793 magnified view (8). Different layers and visualization options can be chosen (9), and
794 the resulting images stored as vector graphics. A binary mask can be defined for each
795 file (10) to exclude tracks (for example, extracellular areas) from further analysis. The
796 mobility analysis via MSD plots is performed based on user-specified parameters (11)
797 and visualized as the mean MSD plot (12), containing the averaged MSD data of the
798 selected file(s). Additionally, the distribution of logarithmized, individual diffusion
799 coefficients (13) is shown, based on the collection of derived diffusion coefficients from
800 fitting the MSD curves of each individual track.

801 **Figure 3. Application of clustering algorithms.**

802 **(A)** Different representations of the same exemplary data set (all localized positions,
803 tracks and track centroids), and visualized results of implemented clustering
804 algorithms. **(B)** GUI of OneFlowTraX for the cluster analysis. The user can choose
805 from several clustering algorithms (14) and set their specific parameters (15). The
806 visualization of the results (16) depends on the chosen method and can be adjusted
807 with several options (17), (18). For some algorithms, parameter estimates can be
808 calculated (19) based on the chosen data.

809 **Figure 4. Workflow and batch processing.**

810 **(A)** Schematic overview of the workflow steps in the GUI of the software and the batch
811 analysis. The GUI is intended to find a suitable set of parameters for all analysis steps,
812 supported by the visualization of intermediate results. The collected parameters can
813 then be used in the batch analysis, which quickly performs all analysis steps for each
814 input file and saves all relevant data in one comprehensive results file. The measured
815 fitting times per file were achieved using an AMD Ryzen 5 4500 CPU and a GTX 960
816 consumer graphics card **(B)** GUI of OneFlowTraX for the batch analysis. All user-
817 specified parameters from all previous tabs are stored in a systematic overview
818 window (20) that can be opened from any tab. Input files for batch processing are also
819 added here and are shown as tables (21) for inspection and the assignment of noise
820 files and masks. The entire file list can then be automatically processed, beginning
821 with the localization procedure and may include tracking, mobility and cluster analysis
822 as chosen by the user, summarized in (22). All parameters and results are stored in a
823 spreadsheet file, a section of which is shown as the inset (23).

824 **Figure 5. BRI1 and RLP44 FP fusions accumulate in the PM of transiently**
825 **transformed *N. benthamiana* epidermal leaf cells or transgenic *A. thaliana***
826 **epidermal hypocotyl cells, respectively, and their nanoscale organization can**
827 **be evaluated by OneFlowTraX.**

828 **(A)** Representative images from sptPALM movies, showing, from left to right, single
829 mEos3.2, PA-GFP and PATagRFP of BRI1 in transiently transformed *N. benthamiana*
830 leaf epidermal cells and of RLP44 in light-grown transgenic *A. thaliana* hypocotyl
831 epidermal cells. The BRI1 and RLP44 fusion proteins were expressed via their native
832 promoters (pBRI1, pRLP44). Scale bar = 1 µM. **(B)** Representative magnifications of
833 areas containing tracks generated by OneFlowTraX (random coloring per track) after

834 localization of the BRI1 and RLP44 fusion proteins, with panels ordered as above.
835 Scale bar = 100 nm. **(C)** Diffusion coefficients for the indicated BRI1) and RLP44
836 fusion proteins in the PM obtained with OneFlowTraX. For statistical evaluation, the
837 data were checked for normal distribution and unequal variances and then analyzed
838 applying the Kruskal-Wallis test followed by the Steel-Dwass post-hoc test, with n ≥ 12
839 for each fusion protein derived from at least five plants, measured on at least three
840 different days. Whiskers show the data range excluding outliers, while the boxes
841 represent the 25-75 percentile. For detailed statistics see Supplemental Table 3.
842 **(D)** The track data was used for cluster analysis in OneFlowTraX, exemplified for
843 BRI1-mEos3.2 and RLP44-mEos3.2 clusters that were assigned using the NASTIC
844 algorithm. The images represent one cell with random coloring per track and cluster
845 boundaries highlighted in white. Scale bar = 2 µm (500 nm for the magnified view).

846 **Figure 6. OneFlowTraX analysis of sptPALM data reveals organ- and position-**
847 **specific as well as environmentally caused differences in the dynamics of the**
848 **indicated FP fusion proteins in epidermal cells of *A. thaliana*.**

849 **(A)** Diffusion coefficients of *pPIP2;1* expressed LTi6a-mEos2 and PIP2;1-mEos2 in
850 epidermal root and hypocotyl cells of light-grown *A. thaliana* seedlings. For statistical
851 evaluation, the data were checked for normal distribution and unequal variances and
852 then analyzed applying the Kruskal-Wallis test followed by the Steel-Dwass post-hoc
853 test, with n ≥ 37 for each fusion protein derived from at least six plants, measured on
854 at least four different days. Whiskers show the data range excluding outliers, while the
855 boxes represent the 25-75 percentile. For detailed statistics see Supplemental Table
856 3. **(B)** Diffusion coefficients of *pRLP44* expressed RLP44-mEos3.2 in epidermal
857 hypocotyl cells of light-grown and dark-grown *A. thaliana* seedlings. The locations of
858 the recorded measurements are indicated by arrows in the corresponding seedling
859 sketches. For dark-grown seedlings, the center of the distance from the apical hook to
860 the seed was used as the reference point. Based on this, the centers to the apical
861 hook and to the seed were used as selected regions, named ‘upper’ and ‘lower’,
862 respectively. Statistical evaluation was performed as described in (A) with n ≥ 14, from
863 at least three plants. For detailed statistics see Supplemental Table 3. **(C)** Diffusion
864 coefficients of *pRLP44* expressed RLP44-mEos3.2 recorded from epidermal
865 hypocotyl cells of light-grown or dark-grown *A. thaliana* seedlings after 20 min
866 treatment with sorbitol solution of 100 mM or 300 mM or after mock-treatment (0 mM).

867 For the recording of the data in the dark-grown seedlings the upper part of the
868 hypocotyl cells was chosen (see (B)). Statistical evaluation was performed as
869 described in (A), with $n \geq 13$, from three different plants. For detailed statistics see
870 Supplemental Table 3.

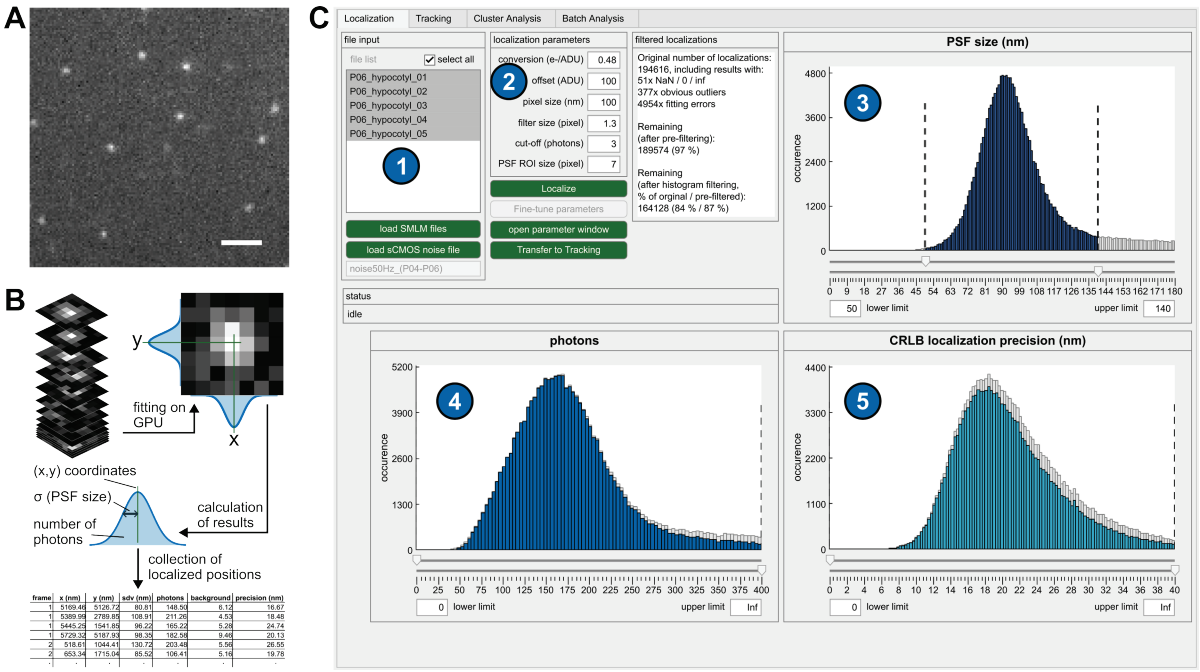

Figure 1. Single-molecule localization procedure.

(A) Single frame of a typical sptPALM image stack. Scale bar = 2 µm. **(B)** Localization process. Each putative single molecule position is cut out as a larger section and fitted with a two-dimensional Gaussian function. The fitting results (most importantly, the coordinates) for each detected single molecule are stored as lists. **(C)** Graphical user interface (GUI) of OneFlowTraX for the localization step. After loading in the sptPALM files (1), the localization procedure is executed based on user-defined parameters (2), with its results visualized as three histograms (PSF sizes (3), photon numbers (4) and localization precision (5)) for all detected and fitted fluorescence spots. This serves as quality control and allows the user to filter out, e.g., badly localized single-molecule positions.

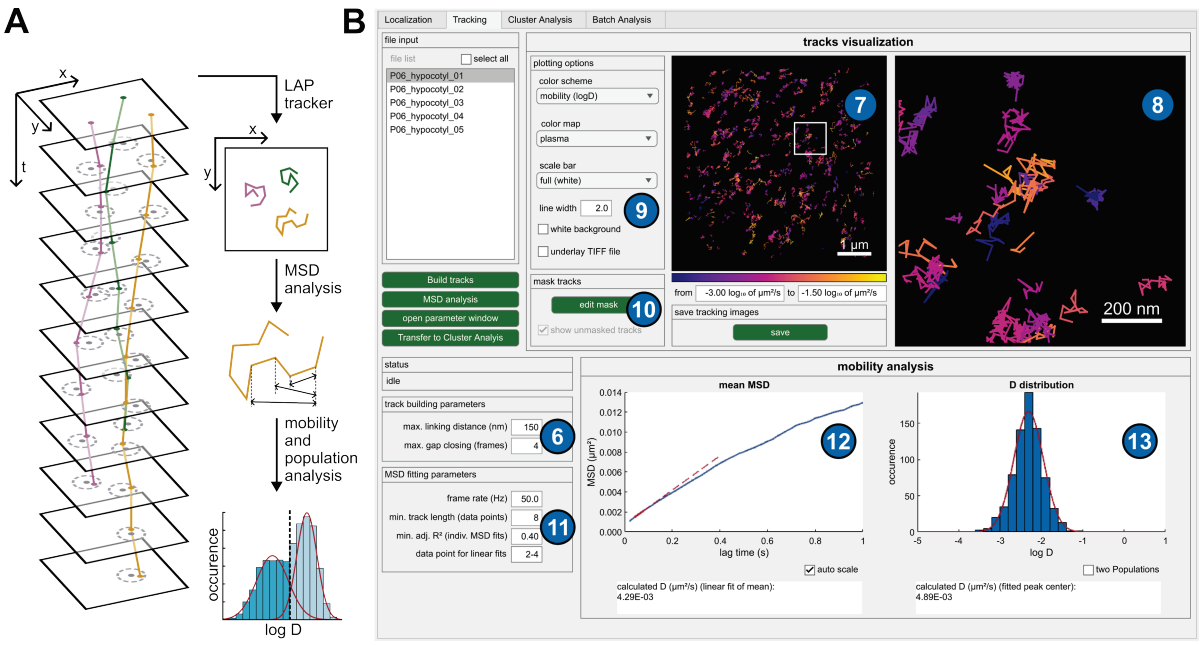

Figure 2. Tracking procedure and mobility analysis.

(A) Schematic overview of the tracking procedure and subsequent analyses. Single-molecule positions are connected to trajectories when they do not exceed a maximum distance (dashed circles) in subsequent frames. The Linear Assignment Problem (LAP) tracker uses a global optimization and can also deal with detection gaps. All tracks then undergo mean square displacement (MSD) analysis based on averaged traveled distances for certain time intervals, offering mobility metrics like diffusion coefficients and more extensive evaluations such as population analyses. **(B)** GUI of OneFlowTraX for the tracking step, including mobility analysis. The track building algorithm uses the specified parameters (6) to connect the detected localization to trajectories, which are displayed in the overview image (7) and a user-defined magnified view (8). Different layers and visualization options can be chosen (9), and the resulting images stored as vector graphics. A binary mask can be defined for each file (10) to exclude tracks (for example, extracellular areas) from further analysis. The mobility analysis via MSD plots is performed based on user-specified parameters (11) and visualized as the mean MSD plot (12), containing the averaged MSD data of the selected file(s). Additionally, the distribution of logarithmized, individual diffusion coefficients (13) is shown, based on the collection of derived diffusion coefficients from fitting the MSD curves of each individual track.

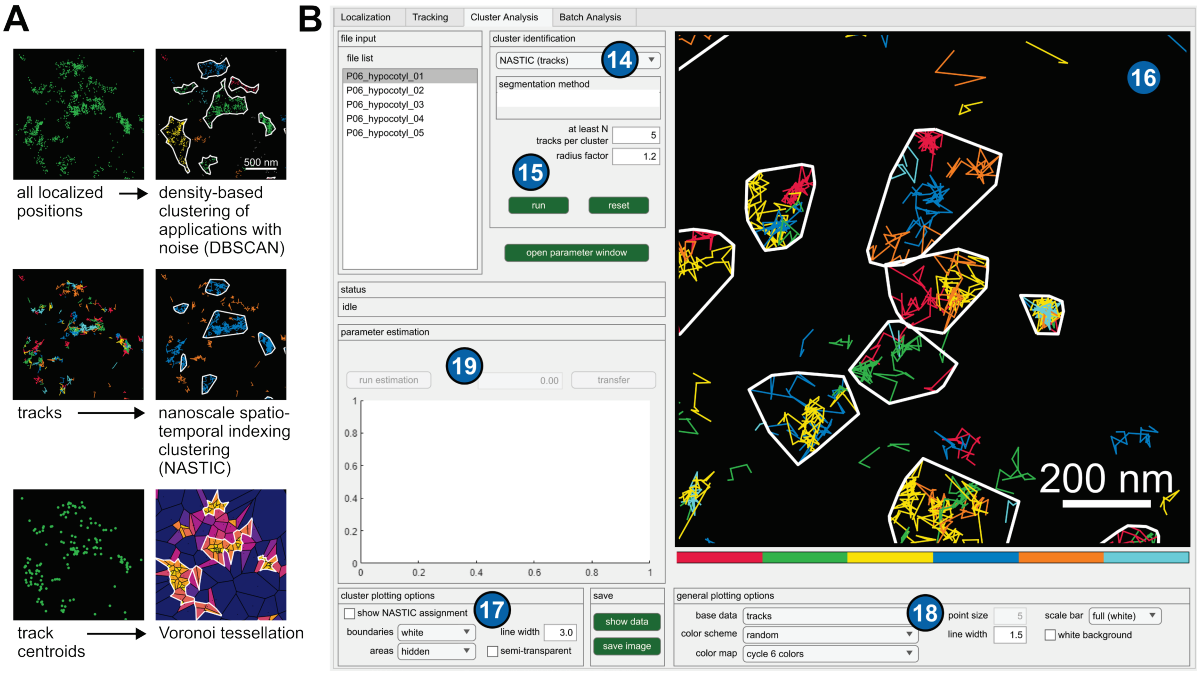

Figure 3. Application of clustering algorithms.

(A) Different representations of the same exemplary data set (all localized positions, tracks and track centroids), and visualized results of implemented clustering algorithms. **(B)** GUI of OneFlowTraX for the cluster analysis. The user can choose from several clustering algorithms (14) and set their specific parameters (15). The visualization of the results (16) depends on the chosen method and can be adjusted with several options (17), (18). For some algorithms, parameter estimates can be calculated (19) based on the chosen data.

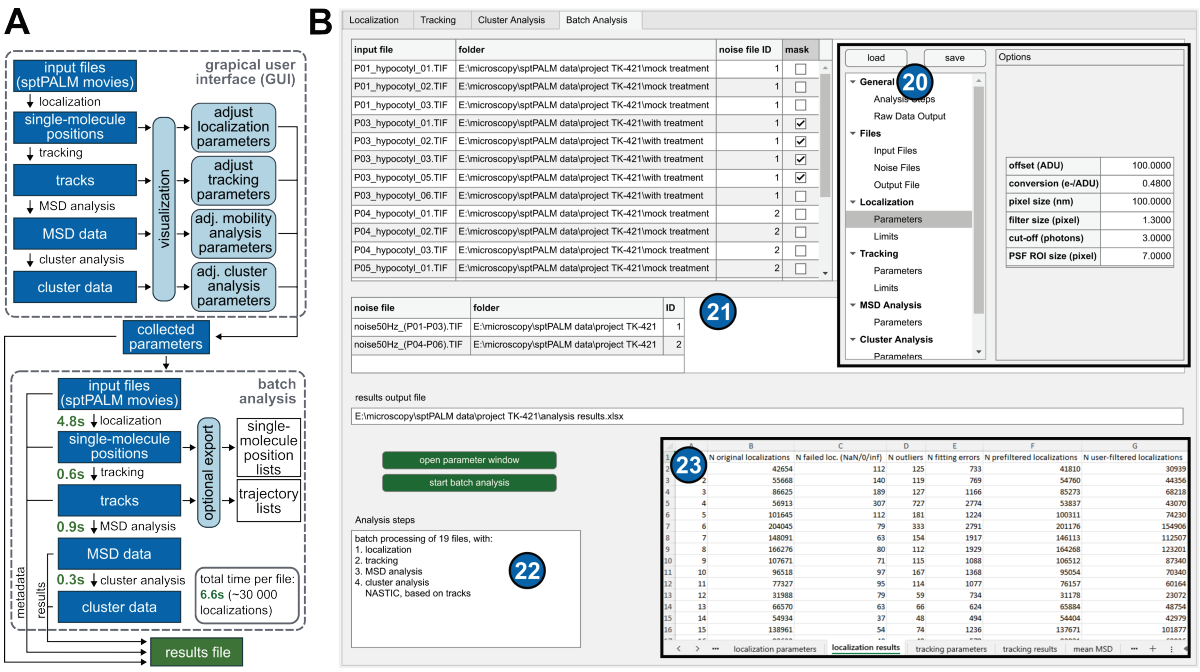

Figure 4. Workflow and batch processing.

(A) Schematic overview of the workflow steps in the GUI of the software and the batch analysis. The GUI is intended to find a suitable set of parameters for all analysis steps, supported by the visualization of intermediate results. The collected parameters can then be used in the batch analysis, which quickly performs all analysis steps for each input file and saves all relevant data in one comprehensive results file. The measured fitting times per file were achieved using an AMD Ryzen 5 4500 CPU and a GTX 960 consumer graphics card **(B)** GUI of OneFlowTraX for the batch analysis. All user-specified parameters from all previous tabs are stored in a systematic overview window (20) that can be opened from any tab. Input files for batch processing are also added here and are shown as tables (21) for inspection and the assignment of noise files and masks. The entire file list can then be automatically processed, beginning with the localization procedure and may include tracking, mobility and cluster analysis as chosen by the user, summarized in (22). All parameters and results are stored in a spreadsheet file, a section of which is shown as the inset (23).

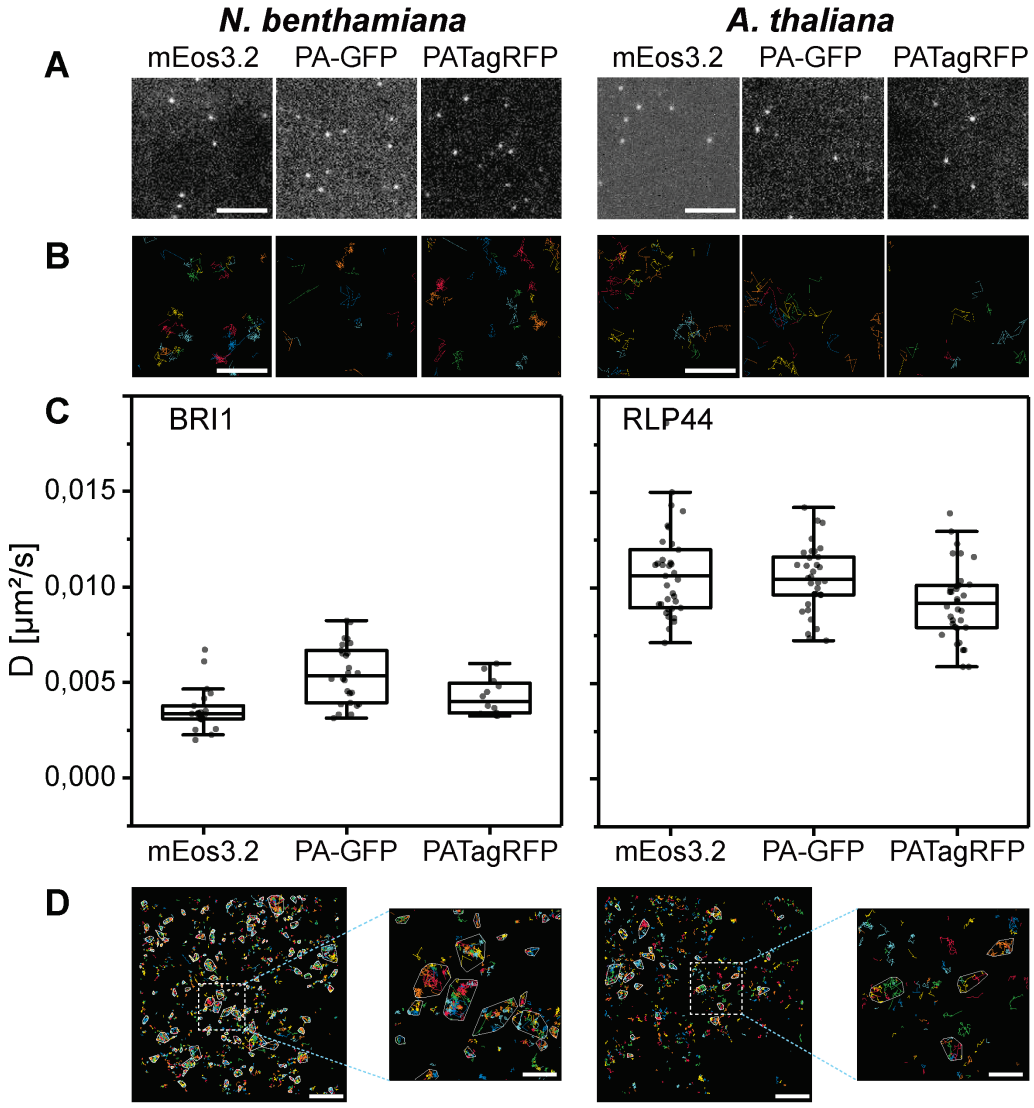

Figure 5. BRI1 and RLP44 FP fusions accumulate in the PM of transiently transformed *N. benthamiana* epidermal leaf cells or transgenic *A. thaliana* epidermal hypocotyl cells, respectively, and their nanoscale organization can be evaluated by OneFlowTraX.

(A) Representative images from sptPALM movies, showing, from left to right, single mEos3.2, PA-GFP and PATagRFP of BRI1 in transiently transformed *N. benthamiana* leaf epidermal cells and of RLP44 in light-grown transgenic *A. thaliana* hypocotyl epidermal cells. The BRI1 and RLP44 fusion proteins were expressed via their native promoters (pBRI1, pRLP44). Scale bar = 1 µM. **(B)** Representative magnifications of areas containing tracks generated by OneFlowTraX (random coloring per track) after localization of the BRI1 and RLP44 fusion proteins, with panels ordered as above. Scale bar = 100 nm. **(C)** Diffusion coefficients for the indicated BRI1) and RLP44 fusion proteins in the PM obtained with OneFlowTraX. For statistical evaluation, the data were checked for normal distribution and unequal variances and then analyzed applying the Kruskal-Wallis test followed by the Steel-Dwass post-hoc test, with n ≥ 12 for each fusion protein derived from at least five plants, measured on at least three different days. Whiskers show the data range excluding outliers, while the boxes represent the 25-75 percentile. For detailed statistics see Supplemental Table 3. **(D)** The track data was used for cluster analysis in OneFlowTraX, exemplified for BRI1-mEos3.2 and RLP44-mEos3.2 clusters that were assigned using the NASTIC algorithm. The images represent one cell with random coloring per track and cluster boundaries highlighted in white. Scale bar = 2 µm (500 nm for the magnified view).

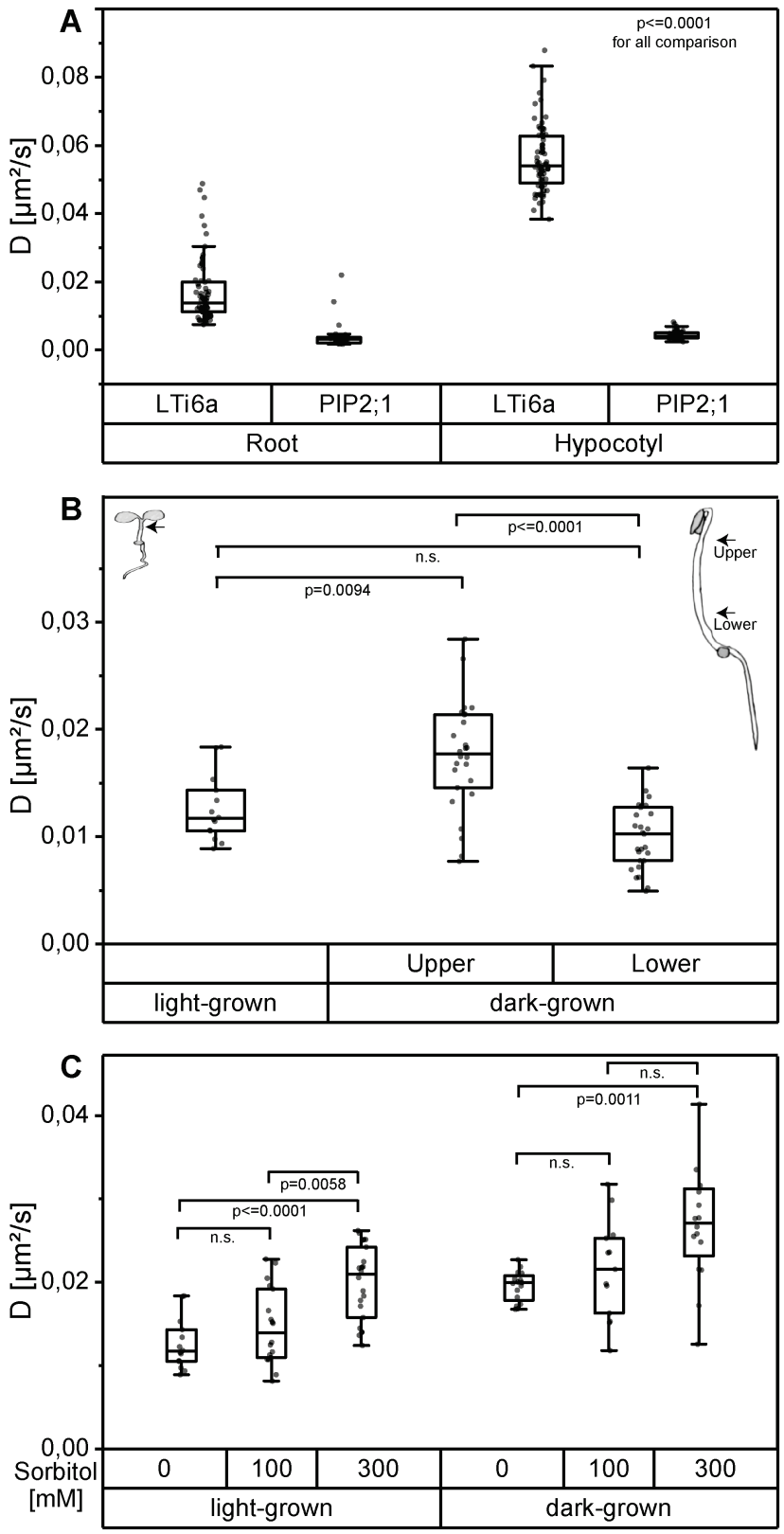

Figure 6. OneFlowTraX analysis of sptPALM data reveals organ- and position-specific as well as environmentally caused differences in the dynamics of the indicated FP fusion proteins in epidermal cells of *A. thaliana*.

(A) Diffusion coefficients of *pPIP2;1* expressed LTi6a-mEos2 and PIP2;1-mEos2 in epidermal root and hypocotyl cells of light-grown *A. thaliana* seedlings. For statistical evaluation, the data were checked for

950 normal distribution and unequal variances and then analyzed applying the Kruskal-Wallis test followed
951 by the Steel-Dwass post-hoc test, with n ≥ 37 for each fusion protein derived from at least six plants,
952 measured on at least four different days. Whiskers show the data range excluding outliers, while the
953 boxes represent the 25-75 percentile. For detailed statistics see Supplemental Table 3. **(B)** Diffusion
954 coefficients of *pRLP44* expressed RLP44-mEos3.2 in epidermal hypocotyl cells of light-grown and dark-
955 grown *A. thaliana* seedlings. The locations of the recorded measurements are indicated by arrows in
956 the corresponding seedling sketches. For dark-grown seedlings, the center of the distance from the
957 apical hook to the seed was used as the reference point. Based on this, the centers to the apical hook
958 and to the seed were used as selected regions, named 'upper' and 'lower', respectively. Statistical
959 evaluation was performed as described in (A) with n ≥ 14, from at least three plants. For detailed
960 statistics see Supplemental Table 3. **(C)** Diffusion coefficients of *pRLP44* expressed RLP44-mEos3.2
961 recorded from epidermal hypocotyl cells of light-grown or dark-grown *A. thaliana* seedlings after 20 min
962 treatment with sorbitol solution of 100 mM or 300 mM or after mock-treatment (0 mM). For the recording
963 of the data in the dark-grown seedlings the upper part of the hypocotyl cells was chosen (see (B)).
964 Statistical evaluation was performed as described in (A), with n ≥ 13, from three different plants. For
965 detailed statistics see Supplemental Table 3.

966 **Supplemental Information**

967 # OneFlowTraX: A User-Friendly Software for Super-Resolution Analysis of
968 # Membrane Protein Dynamics and Nanoscale Organization in Plants

969 Leander Rohr[1], Alexandra Ehinger[1], Luiselotte Rausch[1], Nina Glöckner Burmeister[2],
970 Alfred J. Meixner[3], Klaus Harter[1], Birgit Kemmerling[1], and Sven zur Oven-Krockhaus[1,3,*]

971 [1] Center for Plant Molecular Biology (ZMBP), University of Tübingen, 72076 Tübingen, Germany

972 [2] Department of Biomedicine, Aarhus University, 8000 Aarhus, Denmark

973 [3] Institute for Physical and Theoretical Chemistry, University of Tübingen, 72076 Tübingen, Germany

974

975 *Correspondence: Sven zur Oven-Krockhaus (sven.zur-oven-krockhaus@uni-tuebingen.de)

976

977 **This supplemental information file contains:**

978 **Supplementary Tables 1-5**

979 **Supplementary Figure 1**

980 **Supplementary Materials and Methods**

981

982 # SUPPLEMENTARY TABLES

983 **Supplemental Table 1. Photophysical characteristics of the fluorophores mEos2, mEos3.2,**
984 **PA-GFP and PATagRFP.**

985 For the mEos fluorophores, both the native green (G) and the photoconverted red (R) form are listed,
986 while for PA-GFP and PATagRFP, only the activated forms are presented. The molar attenuation
987 coefficient (ε) refers to the excitation maximum, brightness is the product QY·ε (for comparison: EGFP
988 features a brightness of 33.6 mM^{-1} cm^{-1}). Mean label density was compared in HeLa cells. Note that
989 according to the referenced publication, the high label density of mEos3.2 (compared with mEos2) is
990 likely due to its better maturation and folding properties.

	mEos2 (G)	mEos2 (R)	mEos3.2 (G)	mEos3.2 (R)	PA-GFP	PATagRFP
Excitation maximum (nm)	506	573	507	572	504	562
Emission maximum (nm)	519	584	516	580	517	595
Quantum yield	0.84	0.47	0.84	0.55	0.79	0.38
ε (M^{-1} cm^{-1})	56 000	41 300	63 400	32 200	17 400	66 000
Brightness (mM^{-1} cm^{-1})	47	19	53	18	14	25
pH stability (pK_a)	5.6	6.0	5.4	5.8	n.d.	5.3
Photostability $t_{½}$ (s)	14.0	48.0	12.6	48.0	n.d.	180
Oligomerisation K_d (μM)	20	20	-	-	-	-
Mean label density ($μm^{-2}$)	n.d.	2 649	n.d.	9 865	n.d.	n.d.
Reference for measured values	(Zhang et al., 2012)	(Zhang et al, 2012)	(Zhang et al, 2012)	(Zhang et al, 2012)	(Patterson and Lippincott-Schwartz, 2002)	(Subach et al., 2010)

991

992 **Supplemental Table 2. Nucleotide sequences of the codon-optimized fluorophores mEos3.2,**
993 **PA-GFP and PATagRFP.**

994 Shown are the codon optimized nucleotide sequences of the fluorophores mEos3.2, PA-GFP and
995 PATagRFP and the respective position. Genes were synthesized by Invitrogen's GeneArt services
996 (Thermo Fisher Scientific)

mEos3.2

```
1       ATG TCT GCT ATC AAG CCT GAT ATG AAG ATC AAG CTC AGG ATG GAA GGT AAC
52      GTG AAC GGA CAC CAC TTC GTG ATC GAT GGT GAT GGA ACT GGA AAG CCT TTC
103     GAG GGA AAG CAG TCT ATG GAT CTT GAG GTG AAA GAG GGT GGA CCT CTC CCT
154     TTC GCT TTC GAT ATT CTC ACT ACC GCT TTC CAC TAC GGA AAC AGG GTG TTC
205     GCT AAG TAC CCT GAT AAC ATC CAG GAT TAC TTC AAG CAG TCT TTC CCA AAG
256     GGA TAC TCT TGG GAG AGA TCA CTC ACC TTC GAG GAT GGT GGA ATC TGC AAC
307     GCT AGG AAC GAT ATT ACT ATG GAA GGT GAT ACC TTC TAC AAC AAG GTG AGG
358     TTC TAC GGA ACT AAC TTC CCT GCT AAC GGA CCT GTG ATG CAG AAA AAG ACT
409     CTC AAG TGG GAG CCT TCT ACC GAG AAG ATG TAC GTG AGA GAT GGT GTG CTC
460     ACT GGT GAT ATT GAG ATG GCA CTT CTC TTG GAG GGA AAC GCT CAC TAC AGA
511     TGC GAT TTC AGG ACC ACC TAC AAG GCT AAA GAA AAG GGT GTG AAG CTC CCT
562     GGT GCT CAC TTC GTT GAT CAT TGC ATC GAG ATC CTC TCA CAC GAT AAG GAT
613     TAC AAC AAA GTT AAG CTC TAC GAG CAC GCT GTG GCT CAT TCT GGA CTT CCA
664     GAT AAC GCT AGA AGA TAA
```

PA-GFP

```
1       ATG GTG AGC AAG GGC GAA GAG TTG TTC ACT GGT GTT GTT CCT ATC CTC GTT
52      GAG CTT GAC GGT GAT GTG AAC GGG CAT AAG TTC TCC GTT TCT GGT GAA GGT
103     GAG GGT GAT GCT ACT TAC GGA AAG CTC ACC CTC AAG TTC ATC TGT ACC ACT
154     GGA AAG CTC CCT GTG CCT TGG CCT ACT CTC GTT ACC ACT TTC TCT TAC GGG
205     GTG CAA TGC TTC AGC AGA TAC CCT GAT CAT ATG AAG CAG CAC GAC TTC TTC
256     AAG AGC GCT ATG CCT GAG GGA TAC GTG CAA GAG AGA ACC ATT TTC TTC AAG
307     GAC GAC GGG AAC TAC AAG ACC AGA GCT GAG GTT AAG TTC GAA GGT GAC ACC
358     CTC GTG AAC AGG ATC GAG CTT AAG GGC ATC GAC TTC AAA GAG GAC GGA AAC
409     ATC CTC GGG CAC AAG TTG GAG TAC AAC TAC AAC AGC CAC AAC GTG TAC ATC
460     ATG GCC GAC AAG CAG AAG AAC GGC ATC AAG GCC AAC TTC AAG ATC AGG CAC
511     AAC ATC GAG GAT GGC TCT GTT CAG CTC GCT GAT CAT TAC CAG CAG AAC ACC
562     CCT ATT GGA GAT GGA CCT GTT CTT CTC CCT GAC AAC CAC TAC CTT AGC CAC
613     CAG AGC AAG TTG AGC AAG GAC CCT AAT GAG AAG AGG GAC CAC ATG GTG CTC
664     TTG GAG TTT GTT ACT GCT GCT GGA ATC ACC CTC GGA ATG GAC GAG CTT TAC
715     AAG TGA
```

PATagRFP

```
1      ATG GAA CTC ATC AAA GAA AAC ATG CAC ATG AAG CTC TAC ATG GAA GGG ACC
52     GTG AAC AAC CAC CAT TTC AAG TGC ACA AGC GAA GGT GAG GGA AAG CCT TAC
103    GAG GGA ACT CAG ACC ATG AGA ATC AAG GTG GTG GAA GGT GGA CCT CTT CCT
154    TTC GCC TTC GAT ATT CTC GCC ACC TCC TTC ATG TAC GGG TCC TCT ACT TTC
205    ATC AAC CAC ACT CAG GGA ATC CCG GAC TTC TGG AAG CAA TCT TTT CCA GAG
256    GGA TTC ACC TGG GAG AGA GTG ACT ACT TAC GAG GAT GGT GGT GTG CTC ACT
307    GCT ACT CAG GAT ACT TCT CTT CAG GAC GGC TGC CTC ATC TAC AAC GTG AAG
358    ATC AGA GGT GTG AAC TTC CCG TCT AAC GGA CCG GTG ATG AAG AAA AAG ACT
409    CTC GGA TGG GAG CCG TCT ACC GAG AAA CTT AAG CCT GCT GAT GGT GGA CTT
460    GAG GGA AGA GTT GAC ATG GCT CTT AAG CTC GTT GGA GGT GGA CAT CTC ATC
511    TGC AAC TTC AAG ACC ACC TAC AGG TCT AAG AAG CCG GCC AAG AAC CTT AAG
562    ATG CCT GGG GTT TAC TAC GTG GAC AGG CGT CTT GAG ATT ATC AAA GAG GCC
613    GAC AAA GAG ACT TAC TGG GAG CAG CAT GAA GTG GCT GTG GCT AGG TAT TCT
664    GAC CTT CCA TCT AAG CTC GGG CAC AAG CTC AAT TGA
```

997

998 **Supplemental Table 3. Statistical information about applied tests for the respective figures.**

999 All protein fusions or treatment conditions are listed with the number of replicates (n) and the median
1000 diffusion coefficient (in µm²/s). In addition, all compared combinations and the corresponding p-value
1001 based on the applied test, are shown.

Figure 5 (*N. benthamiana*)

Protein fusion	n	Median diffusion coefficient [µm²/s]
BRI1-mEos3.2	21	0.0033
BRI1-PA-GFP	21	0.0053
BRI1-PATagRFP	12	0.0040

Comparisons Figure 5 (*N. benthamiana*)

Protein 1	Protein 2	p-Value	Applied test
BRI1-mEos3.2	BRI1-PA-GFP	0.0002	Kruskal-Wallis, Steel-Dwass
BRI1-mEos3.2	BRI1-PATagRFP	0.0797	
BRI1-PA-GFP	BRI1-PATagRFP	0.0505	

Figure 5 (*A. thaliana*)

Protein fusion	n	Median diffusion coefficient [µm²/s]
RLP44-mEos3.2	35	0.0106
RLP44-PA-GFP	34	0.0105
RLP44-PATagRFP	34	0.0092

Comparisons Figure 5 (A. thaliana)

Protein 1	Protein 2	p-Value	Applied test
RLP44-mEos3.2	RLP44-PA-GFP	0.9703	Kruskal-Wallis, Steel-Dwass
RLP44-mEos3.2	RLP44-PATagRFP	0.0181	
RLP44-PA-GFP	RLP44-PATagRFP	0.0180	

Figure 6A

Set	n	Median diffusion coefficient [µm²/s]
LTi6a-mEos2 - Root	70	0.0139
PIP2;1-mEos2 - Root	37	0.0032
LTi6a-mEos2 - Hypocotyl	68	0.0540
PIP2;1-mEos2 - Hypocotyl	63	0.0042

Comparisons Figure 6A

Set 1	Set 2	p-Value	Applied test
LTi6a-mEos2 - Root	PIP2;1-mEos2 - Root	≤ 0.0001	Kruskal-Wallis, Steel-Dwass
LTi6a-mEos2 - Root	LTi6a-mEos2 - Hypocotyl	≤ 0.0001	
LTi6a-mEos2 - Root	PIP2;1-mEos2 - Hypocotyl	≤ 0.0001	
PIP2;1-mEos2 - Root	LTi6a-mEos2 – Hypocotyl	≤ 0.0001	
PIP2;1-mEos2 - Root	PIP2;1-mEos2 - Hypocotyl	≤ 0.0001	
PIP2;1-mEos2 - Hypocotyl	LTi6a-mEos2 - Hypocotyl	≤ 0.0001	

Figure 6B

Set	n	Median diffusion coefficient [µm²/s]

Light	14	0.0117
Dark, upper	26	0,0177
Dark, lower	27	0,0103

Comparisons Figure 6B

Set 1	Set 2	p-Value	Applied test
Light	Dark, upper	0.0094	Kruskal-Wallis, Steel-Dwass
Light	Dark, lower	0.0604	
Dark, upper	Dark, lower	≤ 0.0001	

Figure 6C

Set	n	Median diffusion coefficient [µm²/s]
Light, 0 mM	14	0.0117
Light, 100 mM	18	0.0139
Light, 300 mM	22	0.0209
Dark, 0 mM	16	0.0199
Dark, 100 mM	13	0.0215
Dark, 300 mM	16	0.0271

Comparisons Figure 6C (light and dark evaluated separately)

Set 1	Set 2	p-Value	Applied test
Light, 0 mM	Light, 100 mM	0.3683	Kruskal-Wallis, Steel-Dwass
Light, 0 mM	Light, 300 mM	≤ 0.0001	
Light, 100 mM	Light, 300 mM	0.0058	
Dark, 0 mM	Dark, 100 mM	0.6686	
Dark, 0 mM	Dark, 300 mM	0.0011	
Dark, 100 mM	Dark, 300 mM	0.0687	

1002

1003 **Supplemental Table 4. List of sptPALM acquisition and analysis parameters.**

	N. benthamiana constructs with			*A. thaliana* constructs with		
	mEos3.2	PA-GFP	PATagRFP	mEos3.2	PA-GFP	PATagRFP
acquisition						
Power 405 nm (µW)	<15	<15	<15	<20	<20	<40
Power 488 nm (µW)		600			900	
Power 561 nm (µW)	1800		1300	1800		2000
frame rate (Hz)	20	20	20	50	20	20
number of frames	2500-5000	2500-5000	2500-5000	5000	2500	2500
localization						
conversion	0.48	0.48	0.48	0.48	0.48	0.48
offset	100	100	100	100	100	100
pixel size	100	100	100	100	100	100
filter size	1.2	1.2	1.2	1.2	1.3	1.3
cut-off	3	3	3	3	3.5	4
PSF ROI size	7	7	7	7	7	7
tracking						
max. linking distance	200	200	200	200	200	200
max. gap frames	4	4	4	4	4	4
mobility analysis						
min. number of datapoints	8	8	8	8	8	8
number of points for linear fit	4	4	4	4	4	4
adj. R^2 fit threshold value	0.4	0.4	0.4	0.4	0.4	0.4

1004

1005 **Supplemental Table 5. List of constructs.**

1006 All used constructs are listed with our internal numbering, their name, their purpose and source.

Internal #	Name	Purpose	Source
B1-E1	pJET1.2_pBRI1	LI A-B Module	this study
4390	pJET1.2_pRLP44	LI A-B Module	this study
B1-E3	pJET1.2_cBRI1	LI B-D Module	this study
4401	pJET1.2_cRLP44	LI B-D Module	this study
4392	pJET1.2_(GS)mEos3.2	LI D-E Module (with Gly/Ser Linker)	this study
4441	pJET1.2_(GA)mEos3.2	LI D-E Module (with Gly/Ala Linker)	this study
B1-D2	pJET1.2_(GS)PA-GFP	LI D-E Module (with Gly/Ser Linker)	this study
B1-C8	pJET1.2_(GS)PATagRFP	LI D-E Module (with Gly/Ser Linker)	this study
4437	pJET1.2_(GA)PA-GFP	LI D-E Module (with Gly/Ala Linker)	this study
4438	pJET1.2_(GA)PATagRFP	LI D-E Module (with Gly/Ala Linker)	this study
4398	pUC57_nosTerm	LI E-F Module	(Binder et al., 2014)
4400	pGEM-T_pFAST	LI F-G Module	this study
4503	pUC57_Hygromycin	LI F-G Module	(Binder et al, 2014)
B1-E8	BB10 -- pBRI1:cBRI1-(GS)mEOS3.2-nosTerm-pFast -- BB10	LII; Expression in *N. benthamiana*	this study
B1-F8	BB10 -- pBRI1:cBRI1-(GS)PA-GFP-nosTerm-pFast -- BB10	LII; Expression in *N. benthamiana*	this study
B1-E9	BB10 -- pBRI1:cBRI1-(GS)PATagRFP-nosTerm-pFast -- BB10	LII; Expression in *N. benthamiana*	this study
4418	BB10 -- pRLP44:cRLP44-(GS)mEOS3.2-nosTerm-pFast -- BB10	LII; Expression in *A. thaliana*; for Figure 6	this study
4446	BB10 -- pRLP44:cRLP44-(GA)mEOS3.2-nosTerm-pFast -- BB10	LII; Expression in *A. thaliana*; for Figure 5	this study
4479	BB10 -- pRLP44:cRLP44-(GA)PA-GFP-nosTerm-pFast -- BB10	LII; Expression in *A. thaliana*; for Figure 5	this study
4494	BB10 -- pRLP44:cRLP44-(GA)PATagRFP-nosTerm-Hygromycin -- BB10	LII; Expression in *A. thaliana*; for Figure 5	this study

1007

SUPPLEMENTARY FIGURES

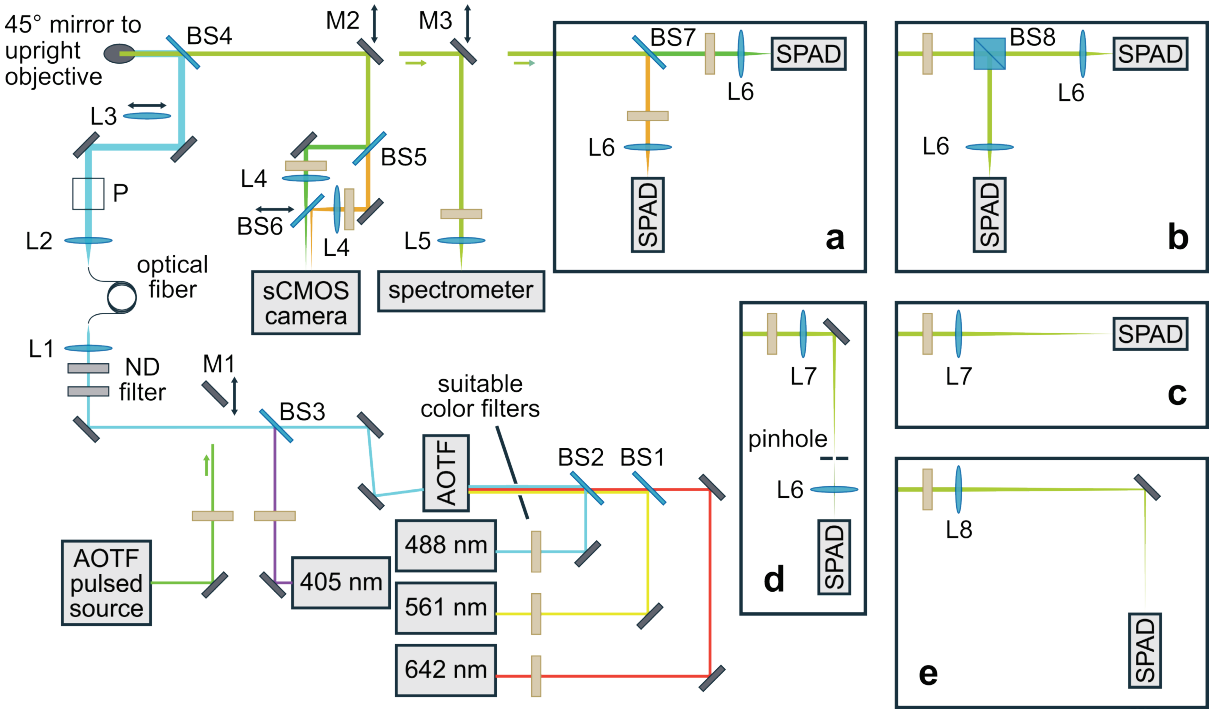

Supplemental Figure 1. Compact schematic overview of the research microscope.

For a detailed description and references to numbered items like lenses (L), beam splitters (BS) and mirrors (M) see text in Supplementary Materials and Methods, also for the different confocal configurations depicted in insets (a-e). Abbreviations: Acousto-optical tuneable filter (AOTF), neutral density filter (ND filter), sCMOS (scientific complementary metal-oxide-semiconductor) camera, single-photon avalanche diode (SPAD). The box P in the beam path denotes the position for additional elements, such as polarization optics. Adapted from (zur Oven-Krockhaus, 2021).

1018 # SUPPLEMENTARY MATERIALS AND METHODS

1019 ## Microscopy

1020 All sptPALM measurements were performed on a custom-built microscope platform,
1021 designed for interdisciplinary research approaches, using different spectromicroscopy
1022 techniques. The following description will therefore also include techniques beyond
1023 sptPALM. A complete description of this microscope and its application in various
1024 research projects can be found in zur Oven-Krockhaus, 2021. References to specific
1025 modules and components refer to Supplemental Figure 1.

1026 ### *Excitation module*

1027 Four different continuous wave (CW) lasers are implemented in the main excitation
1028 path: 405 nm (iBeam smart 405-S-LP, 100mW, Toptica), 488 nm (Oxxius Laserboxx
1029 Diode laser, 100 mW, OXX-488-100, Laser 2000), 561 nm (Vortran Stradus DPSS
1030 laser, 50 mW, VOR-561-050) and 642 nm (Oxxius Laserboxx Diode laser, 130 mW,
1031 OXX-642-130). They cover the most common range of available and utilized
1032 fluorophores. For techniques requiring a pulsed laser source, a supercontinuum fiber
1033 laser (SuperK Extreme EXB-4, with multi-line tunable filter SuperK SELECT UV/VIS-
1034 nIR, both NKT Photonics) is also implemented. Excitation intensities are mainly
1035 controlled by an acousto-optical tuneable filter (AOTF, Polychromatic Modulator 450 -
1036 700 nm, AOTFnC-VIS-TN, with 4-channel RF driver AA.MPDS4C, both AA OPTO-
1037 ELECTRONIC) allowing for the free selection of up to eight laser lines from 400 to 675
1038 nm, which can be used separately as well as in any combination. The CW lasers pass
1039 respective clean-up filters (Laser Clean-Up Filter ZET 405/20, F49-405; Laser Clean-
1040 up Filter ZET 488/10, F49-488; 560/14 BrightLine HC, F39-561; Laser Clean-up Filter
1041 ZET 640/10, F49-643; all AHF analysentechnik AG) and are combined into one beam
1042 path using beam splitters (BS1: Beamsplitter HC BS 555, F38-555; BS2: Laser
1043 Beamsplitter zt 488 RDC, F43-088; BS3: Laser Beamsplitter H 405 LPXR, F48-403;
1044 all AHF analysentechnik AG). Magnetic mirror mounts (M1-3: MDI-HS-3030-M6 on
1045 RD-MP magnetic plates, all Radiant Dyes) are used throughout the setup to change
1046 excitation or emission paths.

1047 ### *Coupling module*

1048 After passing optional neutral density filters, all lasers are coupled into a single mode
1049 fiber (Polarization-Maintaining FC/PC Fiber Optic Patch Cable PM-S405-XP, P1-

405BPM-FC-2, Thorlabs) with aspheric lens L1 (350 - 700 nm, f = 11.0 mm, NA = 0.25 Aspheric Lens, C220TMD-A, Thorlabs) for uniform, spatially cleaned-up Gaussian laser profiles. Fiber de-coupling is done with achromatic lens L2 (Ø1" Achromatic Doublet, ARC: 400-700 nm, f=30 mm, AC254-030-A-ML, Thorlabs) collimating the excitation beam to a diameter of 10 mm. Afterwards, additional optical elements like linear polarizers (Mounted GT Polarizer, 10 mm x 10 mm, 350 - 700 nm AR Coating, GTH10M-A, Thorlabs) and/or retardation plates (Ø1/2" Mounted Achromatic Half-Wave Plate, Ø1" Mount, 400 - 800 nm, AHWP05M-600, Thorlabs) can be introduced to control the polarization for respective experiments (e.g. anisotropy measurements). An xyz-adjustable lens L3 (Ø1" UVFS Plano-Convex Lens, f = 150.0 mm, ARC: 350 - 700 nm, LA4874-A-ML, Thorlabs) can be pushed into the beam path, which focuses on the back focal plane of the microscope objective, thus allowing switching between either confocal, or epi-fluorescence/TIRFM/VAEM illumination. For VAEM, the angle can be adjusted by lateral translation of this lens. Laser excitation is reflected by the multi-band beam splitter BS4 (TIRF Quad zt405/488/561/640rpc, F73-410, AHF analysentechnik AG), and directed upwards by a 45° mirror.

Sample stage

The sample stage mainly consists of a custom-manufactured aluminum frame that holds a piezo table (3-Axis Piezo Scanner with Direct Position Measuring, P-527.3CD, controlled by 3-Axis Digital Piezo Nanopositioning Controller, E-710.3CD, both Physik Instrumente (PI)) for sample-scanning in confocal measurements or small adjustments of the sample position in widefield applications. Laser excitation passes the microscope objective (Objective alpha Plan-Fluar 100x/1,49 Oil M27, 421190-9800-000, Carl Zeiss Microscopy) that can be adjusted in z for focusing onto the sample. An aluminum plate is mounted onto the piezo table with a round recess for the objective, allowing to install different kinds of sample holders. Fluorescence from the sample is collected by the same objective and passes the beam splitter BS4, entering the emission path.

Detection module

Here, light from the main emission beam path can be redirected via removable mirrors M2 and M3 to the individual detectors. For widefield applications, M2 directs the emission to an sCMOS camera (Digital CMOS camera, ORCA-Flash4.0 V2, Hamamatsu Photonics), focused by an achromatic lens (Ø1" Achromatic Doublet,

ARC: 400-700 nm, f=100.0 mm, AC254-100-A-ML, Thorlabs). If needed, green/red channel splitting can be done by the alternative setup shown in Supplemental Figure 1, using beam splitters (BS5: Laser Beamsplitter H 560 LPXR superflat, F48-559; BS6: Shortpass beamsplitter HC BS 556 SP, F38-556; both AHF analysentechnik AG) and two lenses L4 (Biconvex lens; N-BK 7; D=25.4; F=100; mounted, G063854000, Qioptiq) to focus the two emission beams on laterally displaced regions on the camera chip.

For spectroscopy using confocal illumination, the next detector is a spectrograph, consisting of a 30 cm focal length imaging monochromator (Imaging Spectrograph, Acton SP-2356, Princeton Instruments) and a thermoelectrical cooled CCD camera (Digital CCD Camera System, PIXIS 100B, Princeton Instruments), with achromatic lens L5 (Achr. VIS ARB2; D=12.5; F=40; mounted, G052010000, Qioptiq) focusing on the entrance slit.

The following detector block features single-photon avalanche diodes (SPADs, PDM, Micro Photon Devices) for their use in confocal techniques like fluorescence lifetime imaging microscopy (FLIM), fluorescence (lifetime) correlation spectroscopy (F(L)CS), antibunching or other experiments with single-molecule detection. Both SPAD and pulsed laser synchronization signals are fed into a time-correlated single photon counting (TCSPC) module (PicoHarp 300, Picoquant GmbH) to measure the time delay between sample excitation and the arrival of an emitted photon at the detector. Insets a-e in Supplemental Figure 1 describe different configurations using different lenses (L6: Ø1" Achromatic Doublet, ARC: 400-700 nm, f=40.0 mm, AC254-040-A, Thorlabs; L7: Achr. VIS ARB2; D=25.4; F=200; mounted, G063237000, Qioptiq; L8: Achr. VIS ARB2; D=25.4; F=400, G322340322, Qioptiq) for specific experimental setups: (a) dual-color FLIM/F(L)CS with beam splitter BS7 (Laser Beamsplitter H 560 LPXR superflat, F48-559, AHF analysentechnik AG); (b) anisotropy measurements with polarizing beam splitter BS8 (20 mm Polarizing Beamsplitter Cube, 420 - 680 nm, PBS201, Thorlabs); (c) low intensity measurements (no optical sectioning to maximize signal intensity); (d) high-contrast imaging (pinhole for optical sectioning); (e) compromise between (c) and (d), the projected Airy disk is about the size of the SPAD's detector area, effectively excluding most out-of-focus light.

Hardware control

All lasers are controlled (directly and via the AOTF) by a custom-written software in LabVIEW (LabVIEW 2018, National Instruments). A standard PC gaming controller is used for focusing and (for widefield applications) lateral adjustments of the sample position, also written in LabVIEW. Widefield sCMOS camera data is recorded with the HoKaWo software (HoKaWo 3.0, Hamamatsu Photonics), while TCSPC data is acquired with SymPhoTime 64 (SPT64-1+2, Picoquant GmbH).

REFERENCES

Binder, A., Lambert, J., Morbitzer, R., Popp, C., Ott, T., Lahaye, T., and Parniske, M. (2014). A modular plasmid assembly kit for multigene expression, gene silencing and silencing rescue in plants. PLoS One **9**:e88218. https://doi.org/10.1371/journal.pone.0088218.

Patterson, G.H., and Lippincott-Schwartz, J. (2002). A photoactivatable GFP for selective photolabeling of proteins and cells. Science **297**:1873-1877. https://doi.org/10.1126/science.1074952.

Subach, F.V., Patterson, G.H., Renz, M., Lippincott-Schwartz, J., and Verkhusha, V.V. (2010). Bright Monomeric Photoactivatable Red Fluorescent Protein for Two-Color Super-Resolution sptPALM of Live Cells. J. Am. Chem. Soc. **132**:6481-6491. https://doi.org/10.1021/ja100906g.

Zhang, M.S., Chang, H., Zhang, Y.D., Yu, J.W., Wu, L.J., Ji, W., Chen, J.J., Liu, B., Lu, J.Z., Liu, Y.F., et al. (2012). Rational design of true monomeric and bright photoactivatable fluorescent proteins. Nat. Methods **9**:727-729. https://doi.org/10.1038/Nmeth.2021.

zur Oven-Krockhaus, S. (2021). A modular, comprehensive microscopy platform for modern live cell imaging. Thesis. https://doi.org/10.15496/publikation-62250.